**Supplementary Information for:**

# Perovskite superlattices with efficient carrier dynamics

Yusheng Lei[1,2*], Yuheng Li[1*], Chengchangfeng Lu[3], Qizhang Yan[1], Huaxin Gong[2], Song Zhang[2], Jiayun Zhou[4], Ruiqi Zhang[1], Yimu Chen[1], Hsinhan Tsai[5], Yue Gu[4], Hongjie Hu[1], Yu-Hwa Lo[3], Wanyi Nie[5], Taeyoon Lee[6,7], Jian Luo[1,4], Kesong Yang[1], Kyung-In Jang[8], Sheng Xu[1,4,5,9#].

[1]Department of Nanoengineering, University of California San Diego, La Jolla, CA 92093-0448, USA
[2]Department of Chemical Engineering, Stanford University, Stanford, CA 94305, USA
[3]Department of Electrical and Computer Engineering, University of California San Diego, La Jolla, CA 92093, USA
[4]Material Science and Engineering Program, University of California San Diego, La Jolla, CA 92093-0418, USA
[5]Los Alamos National Laboratory, Los Alamos, NM 87545, USA
[6]School of Electrical and Electronic Engineering, Yonsei University, Seoul 03722, Republic of Korea.
[7]Department of Bio and Brain Engineering, Korea Institute of Science and Technology, Republic of Korea.
[8]Department of Robotics Engineering, Daegu Gyeongbuk Institute of Science and Technology, Daegu 42988, Republic of Korea.
[9]Department of Bioengineering, University of California San Diego, La Jolla, CA 92093-0412, USA
[*]These authors contributed equally to this work.
[#]Email: shengxu@ucsd.edu

## Supplementary Discussion 1: Epitaxial superlattice structure.

Low-dimensional perovskites show improved long-term stability due to the hydrophobic organic surface terminating ligands[1] and hysteresis-free electrical transport, probably because of the high exciton binding energy of the multiple-quantum-well[2]. Unlike the traditional 3D metal halide perovskite (e.g., $MAPbBr_3$ and $MAPbI_3$), low-dimensional perovskites are composed of two parts: the inorganic slab and the organic spacer[3]. In the inorganic slab, the structure (metal-halide frameworks and the organic cations) is the same as that of the traditional 3D perovskite. However, because of the existence of the organic spacer (e.g., BA and PEA), the continuous crystal structure in the 3D perovskite is split evenly into periodic two-dimensional (2D) layered structures, which results in a natural multiple-quantum-well. Therefore, the major difference between the 3D and low-dimensional perovskites is the layered organic spacers, which determines the *n* value (the layer of the inorganic slabs) of the chemical formula $B_2A_{n-1}M_nX_{3n+1}$ (e.g., B = $R\text{-}NH_3^+$; A = $CH_3NH_3^+$, $HC(NH_2)_2^+$, $Cs^+$, $Rb^+$; M = $Pb^{2+}$, $Sn^{2+}$; X = $Cl^-$, $Br^-$, $I^-$) for low-dimensional perovskites.

In polycrystals, low-dimensional perovskites cannot form a long-range order due to the misaligned orientations of the inorganic slabs[2,4,5], representing a major limiting factor for achieving highly efficient carrier dynamics[5-9]. Bulk single crystals are valuable for studying fundamental material properties of low-dimensional perovskites but are less useful for building devices that usually require thin films. Thin plates of single-crystal low-dimensional perovskites have been demonstrated[10-12], but due to their natural growth behavior, those thin plates are usually made of large-area inorganic slabs stacking on top of another, so they have only in-plane carrier transport within the slab but not out-of-plane carrier transport between the slabs as required for building high-performance electronic devices[10,11]. Specifically, carriers can transport along the inorganic slabs very efficiently, but when they travel across to the insulative organic spacers, strong recombination and trapping will take place.

The low-dimensional perovskite superlattice reported in this work overcame these challenges. The superlattice could be obtained by a heteroepitaxial growth method (Supplementary Fig. 2). In this epitaxial system, because the substrates were still perovskites, they were able to form strong metal-halide ionic bonds with the inorganic slabs (Fig. 1b)[13-15], which was much stronger than the weak Van der Waals forces between the substrate and the organic spacers in the low-dimensional perovskite layer. In addition, it was also not energy favorable to form horizontal epitaxial layers where a complete organic or inorganic layer was grown on the substrate as the first layer, which would otherwise contain a perovskite layer of an infinite $n$, a thermodynamically unstable structure[16] (Supplementary Fig. 1).

Therefore, the epitaxial layer formed a vertically aligned rather than a horizontally aligned structure (Fig. 1a and 1b; Supplementary Figs. 1, 2, and 3). The vertically aligned structure could be visualized by both SEM and STEM, showing apparent morphology differences from traditional 3D perovskites.

Besides the epitaxial orientation, the as-grown crystals were also found to exhibit a crisscross crystal morphology (Fig. 1a; Supplementary Figs. 2 and 3). The reason originated from the substrate. In this epitaxial process, the substrates in this study (e.g., $MAPb_{0.5}Sn_{0.5}Br_3$) all had a cubic lattice structure[17], suggesting that the lattice parameters in the $a$ and $b$ directions are symmetric. There would not be any differences if the epitaxial crystal plates were growing along the $a$ or $b$ direction. As a result, the chances for the epitaxial crystal plates to grow along the *a* and *b* directions were roughly 50%-50%. Therefore, the as-grown epitaxial layers exhibit two perpendicular crisscross morphologies.

**Supplementary Discussion 2: EBIC mapping.**

We used EBIC mapping to visualize the surface current of different low-dimensional perovskites. The factors that would influence the current include the bandgap and the carrier recombination centers. In Fig. 2d and 2e, the current mapping results from the polycrystalline samples show a non-homogenous feature, indicating that different grains exhibit different carrier collection efficiencies, which is attributed to the random crystal orientations in those grains. Besides, the lowest current signals always appear at the grain boundaries, suggesting that the polycrystalline structure suffers from serious carrier recombination, particularly at the grain boundaries.

In contrast, the epitaxial superlattice samples showed very different signals. Even though the SEM images exhibited flat surface morphologies, the simultaneously captured EBIC signals showed crisscross or linear signal features. Such a phenomenon was from the imperfect crystal merging during the processes of forming the epitaxial thin film, which is almost impossible to avoid due to the thin plate merging. Also, due to the strong lattice strain, the possibility for crystallography defects (e.g., lattice misorientation and dislocations between the organic spacers and the inorganic slabs) was relatively high (Fig. 3b; Supplementary Fig. 11). SEM imaging was based on reflected electrons at the sample surface, while EBIC could collect current signals several micrometers deep into the samples. Therefore, those defects, even though not visible at the surface by SEM, were reflected by the electrical measurements in

EBIC. Additionally, the signal intensity was much higher in the superlattice samples than that in the polycrystals due to the enhanced carrier generation and collection, which were attributed to the reduced energy bandgap (Supplementary Fig. 16) and transport barriers, respectively.

## Supplementary Discussion 3: Lattice strain.

Lattice strains existed in the perovskite single-crystal heterostructures, which were caused by the lattice mismatch between the substrate and the epitaxial layer[13]. In traditional 3D perovskites, the lattice strain was usually very small. Otherwise, the epitaxial layer would not grow at the first place because the large strain energy would significantly increase the barrier for nucleation. However, in low-dimensional perovskites, a large composition is the relatively soft organics. Therefore, the structure becomes more deformable and can tolerate larger strain levels[18-21]. As a result, even though the strain between the inorganic slabs and the substrate was still small, the strain between the organic spacers and the substrate could be much larger.

In the low-dimensional perovskite superlattice, each inorganic slab was epitaxially grown on the substrate through the metal-halide ionic bonds. In this way, the organic spacers (BA, ~0.700 nm when free-standing[22]) in between the inorganic slabs will be compressed by the adjacent inorganic slabs to fit into a single lattice unit (~0.596 nm) of the substrate (Fig. 1b). The organic spacers would not be stretched over two lattice units (~1.192 nm) of the substrate, which otherwise causes too large strain to be thermodynamically stable. Therefore, the overall lattice strain is from two aspects: the inorganic slabs, which is relatively small, and the organic spacers, which is relatively large.

In Figure 3a, the XRD results were used to calculate the overall lattice constants along the *a*, *b*, and *c* directions of the low-dimensional perovskites. The material in those measurements corresponds to $n = 1$. The Sn-I bonds (in conventionally grown single crystals) in the *a-b* plane are treated the same as those in their 3D counterparts[23,24]. Therefore, the first peak (14.66°) in the *a-c/b-c* plane of the conventionally grown single crystal was used to calculate the d-spacing between two Sn atoms. According to Bragg's Law, the calculated d-spacing was ~6.04 nm in both *b* and *c* directions. And the first peak (6.77°) in the *a-b* plane of the conventionally grown single crystal was also used to calculate the d-spacing between two Sn atoms along the *a* direction, resulting in a d-spacing of ~13.04 nm.

Similarly, the first peak (14.50°) in the *a-c/b-c* plane of the superlattice was used to calculate the d-spacings in the *c* direction, ~6.10 nm. Therefore, the tensile strain along the *c* direction is (6.10-6.04)/6.04 = 0.99%. Additionally, the first peak (7.41°) in the *a-b* plane of the superlattice was used to calculate the d-spacings in the *a* direction, ~11.92 nm. Therefore, the compressive strain along the *a* direction is (11.92-13.04)/13.04 ≈ -8.59% strain. Finally, together with the STEM analysis, the compressive strain along the b direction is (6.04-11.92/2)/6.04 = 1.32%.

In the calculations, we only need to use the first peak because the other peaks are the multiple-order diffractions of the first peak.

**Supplementary Discussion 4: The dielectric confinement.**

The low-dimensional perovskites contain alternating inorganic slabs and organic spacers. The dielectric constants of those two parts are very different, where the dielectric constant of the inorganic slabs is much larger than that of the organic spacers, resulting in a strong effect of dielectric confinement[25]. Therefore, due to the largely compressed organic spacers, their dielectric constants were increased, indicating that the difference between the inorganic slabs and the organic spacers was smaller, which resulted in a weakened dielectric confinement effect.

## Supplementary Discussion 5: $Bi^{3+}$ alloying.

The epitaxial growth of low-dimensional perovskites on traditional 3D perovskites introduced enormous lattice strains. Even though the BA could tolerate the structural deformation to a certain extent, the compression from the organic spacers to their adjacent inorganic slabs could still cause the structural failure of the Sn-I slab from their original black phase to a transparent phase in several days (Supplementary Fig. 15). The degradation rate was found to be highly related to the $n$-value in the general formula of low-dimensional perovskites (Supplementary Fig. 14). The smaller the $n$, the more rapid the material degrades.

For example, when $n = 1$, the width of a unit cell in a conventionally grown single crystal (containing one inorganic slab and one BA) is 0.604 nm + 0.7 nm = 1.304 nm, which would be fitted into two unit cells of the 3D perovskite substrate whose width is 0.596 nm + 0.596 nm = 1.192 nm, resulting in an overall epitaxial strain of 8.59% (Supplementary Table. 1). As the $n$ value increases, the volume ratio of the inorganic slab gets larger. Even though the lattice strain between the inorganic slabs and the substrate does not change, the overall epitaxial strain is reduced (Fig. 3b). For $n = 5$, the overall strain is calculated to be 3.87%. Additionally, a high $n$-value inorganic slab can tolerate higher strain levels applied by the organic spacers since there are multiple inorganic layers to help share the strain.

Even though high $n$-value epitaxial layers are more stable, they still underwent phase-change from black to transparent in usually less than 3-5 days (Supplementary Figs. 14, 15, and 19), which was difficult for device fabrication as well as practical applications. Therefore, it was necessary to find a strategy to reduce the strain and improve their stability further.

Reducing the lattice constant of the epitaxial layer by alloying/doping small sized-ions can potentially reduce the strain in the superlattice and thus enhance its stability. $Bi^{3+}$ was chosen as a smaller metal ion to partially replace the $Sn^{2+}$ to release more space for the BA. DFT calculations were carried out to evaluate the effect of $Bi^{3+}$ alloying. The perovskite with $n = 3$ was adopted as a model in this work since it contains both MA and BA, and its structural complexity can be afforded by the computational capacity in this work (Supplementary Fig. 17). Calculation results showed that the $Bi^{3+}$ was more likely to replace the $Sn^{2+}$ close to the BA to achieve lower total energy. When the replacement site was further away from the BA, the total energy became larger. Therefore, $Bi^{3+}$ was preferably concentrated at the BA/inorganic slab interface (Supplementary Fig. 18).

The calculations also revealed that $Bi^{3+}$ alloying vastly changed the band structure (Supplementary Figs. 20 and 21): a much-decreased conduction band minimum (CBM) while the valence band maximum (VBM) did not have any noticeable changes. Therefore, the $Bi^{3+}$ alloying resulted in a double-band structure in the inorganic slabs, where the alloyed Bi/Sn-I region showed a smaller bandgap than the intact Sn-I region, which was highly associated with the strong epitaxial strain, where the $Bi^{3+}$ concentrated at the organic spacer/inorganic slab interface to reduce the lattice strain, which changed the local conduction band edge and formed a double-band structure of the superlattice.

In addition, the $Bi^{3+}$ alloying did not cause a macroscale phase separation between Bi and the Sn components. Even though small peaks appeared in the $Bi^{3+}$ alloyed superlattice (Supplementary Fig. 19), the intensity is considered to be negeligible compared to the strong and narrow peak at ~1000 nm, suggesting the $Bi^{3+}$ alloying superlattice is still uniform in the macroscale. Even though the $Bi^{3+}$ aggregates at the interfaces between the inorganic slabs and the organic spacers, the well-aligned inorganic slabs and organic spacers guarantee the uniform distribution of $Bi^{3+}$ in the entire structure.

**Supplementary Discussion 6: Intra-band exciton relaxation.**

Photovoltaic devices based on the $Bi^{3+}$ alloyed low-dimensional perovskite superlattice were found to exhibit a largely improved $V_{OC}$ (Supplementary Fig. 25). In principle, the $V_{OC}$ of a photovoltaic device was determined by the internal quasi-fermi-level splitting, which always stayed inside the bandgap of the absorber. However, the observed high $V_{OC}$ exceeded the bandgap of the Bi/Sn-I region, which suggests an unusual electron transport process in the superlattice.

To investigate the mechanism, we performed wavelength-dependent *J-V* measurements on both superlattice and polycrystalline devices (Fig. 4d). The polycrystalline devices also contained the same concentration of, but uniformly mixed, $Bi^{3+}$. Even though the same $Bi^{3+}$ concentration was applied, the epitaxial and polycrystalline devices showed different bandgaps. The reason is two-fold: first, the epitaxial and polycrystalline thin films did not have the same structure, strain, or crystallinity. Second, the $Bi^{3+}$ in the epitaxial thin film would concentrate at the organic spacer/inorganic slab interface to form an atomic-level Bi/Sn-I region, where the local concentration of $Bi^{3+}$ should be higher than 10%. However, the $Bi^{3+}$ in the polycrystalline thin films was uniform 10%.

The results of wavelength-dependent *J-V* measurements showed that when increasing the wavelength of the incident light, the shapes of *J-V* curves from the polycrystalline devices were all like each other, while those from the superlattice devices changed a lot. We then extracted the corresponding $V_{OC}$ and *F.F.* to evaluate the carrier collections (Fig. 4e). It showed that the $V_{OC}$ in the polycrystalline devices was maintained to be ~0.5-0.6 V, which was relatively constant at different wavelengths of the incident light, because the band structure of the thin film was uniform. However, the $V_{OC}$ in the superlattice devices kept ~0.7 V when the incident light wavelength was less than ~900 nm and dropped to ~0.45 V when the incident light wavelength was over ~900 nm. Similarly, the *F.F.* of the polycrystalline devices almost kept constant regardless of the wavelength of the incident light because the uniform band structure did not result in different energy barriers. However, the *F.F.* of the superlattice devices began to drop from ~0.7, when the incident light wavelength was at ~800 nm, to an extremely small value of ~0.25 when the incident light wavelength was ~1100 nm. Those results clearly revealed that the excitation energy was critical for the superlattice devices.

Structural computation illustrated that $Bi^{3+}$ ions in the superlattice concentrated at the interface between the inorganic slab and the organic spacer to form an atomic-level alloyed layer. As a result, the superlattice exhibits an additional atomic-level heterostructure. Due to the vertically aligned superlattice structure, the Bi/Sn-I region and the Sn-I region in the inorganic slabs were connected to the electron transport layer (ETL) simultaneously (Fig. 4c). Under excitation, the electrons at the high-energy states could come from both the Bi/Sn-I and the Sn-I regions. During the high-energy electron relaxation process, those electrons generated from the Sn-I region will relax to the Sn-I region to be extracted by the ETL layer. Moreover, those high-energy electrons (higher than the CBM of the Sn-I) generated from the Bi/Sn-I region could also relax, by intra-band diffusion, to the Sn-I region rather than the Bi/Sn-I region.

This process was possible due to two reasons. First, since the energy level of the ETL layer was lower than the CBM of the Sn-I region but higher than that of the Bi/Sn-I region, it was more energy favorable for the electron to transport from the Sn-I region than the Bi/Sn-I region, to the ETL. Second, the atomically thin Bi/Sn-I region led to a short distance of the intra-band diffusion for the high-energy electrons before their rapid relaxation.

In this way, if the excitation energy was higher than the bandgap of the Sn-I region, the $V_{OC}$ magnitude was mainly determined by the energy level of the ETL and the band tail states near the VBM of the Bi/Sn-I region, which is not related to the bandgap of the Bi/Sn-I region. When the excitation energy was less than the bandgap of the Sn-I region but higher than the bandgap of the Bi/Sn-I region, the $V_{OC}$ magnitude was mainly determined by the energy level of the band tail states near the CBM and the band tail states near the VBM in the Bi/Sn-I region, which resulted in a low $V_{OC}$.

Under mixed excitation energies, those high-energy electrons, which are excited by the short-wavelength from both Bi/Sn-I and Sn-I regions to states higher than the CBM of the Sn-I region, are extracted by the ETL, indicating that the quasi-fermi-level splitting is mainly determined by the Sn-I region, which results into a high $V_{OC}$. In the meantime, those low-energy electrons excited by the long-wavelength only exist in the Bi/Sn-I and cannot efficiently transport to the CBM of the Sn-I or the ETL—they could not be either directly extracted by the

ETL or transport to the Sn-I region, indicating that they are not likely to contribute to the photovoltaic device but only increase the carrier population in the conduction band of the Sn-I region. Moreover, their energy and quantity are both low, which minimally impacts the overall $V_{OC}$ of the integrated device.

In contrast, if a Bi/Sn-I based and a Sn-I based photovoltaic devices were fabricated separately and directly connected in parallel by external cables, the overall output voltage of this combined module would be equal to the output voltage of the Bi/Sn-I one since this module would be two standard power sources connected in parallel. In addition, even when two separate photovoltaic devices were in close contact with each other (e.g., as defined by advanced lithography), their absorber material dimensions could not support the inter-band hot carrier transport since the rapid relaxation of the hot carriers would prevent those hot carriers from transporting between the two absorbers of the two devices[26,27]. Therefore, the atomic-level intra-band relaxation process in this work was critical for the unique carrier dynamics, as well as the performance, of the superlattice photovoltaics (Supplementary Fig. 26).

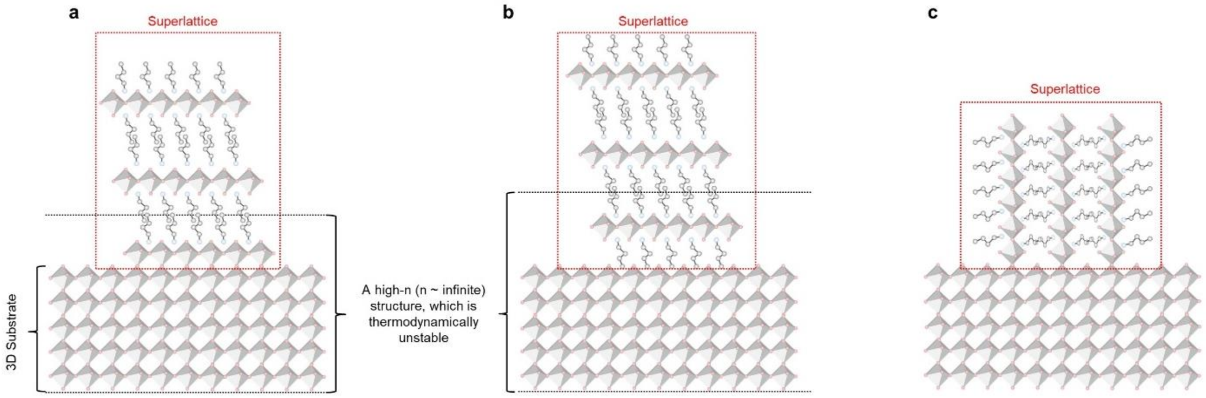

**Supplementary Fig. 1 | Schematics of different epitaxial models.** Both models (**a**) and (**b**) could be considered to contain an infinite *n*-value perovskite layer, which is thermodynamic unstable. Only model (**c**) could form strong coherent metal-halide bonds between the substrate and the epitaxial layer while holding thermodynamic stable small *n*-values.

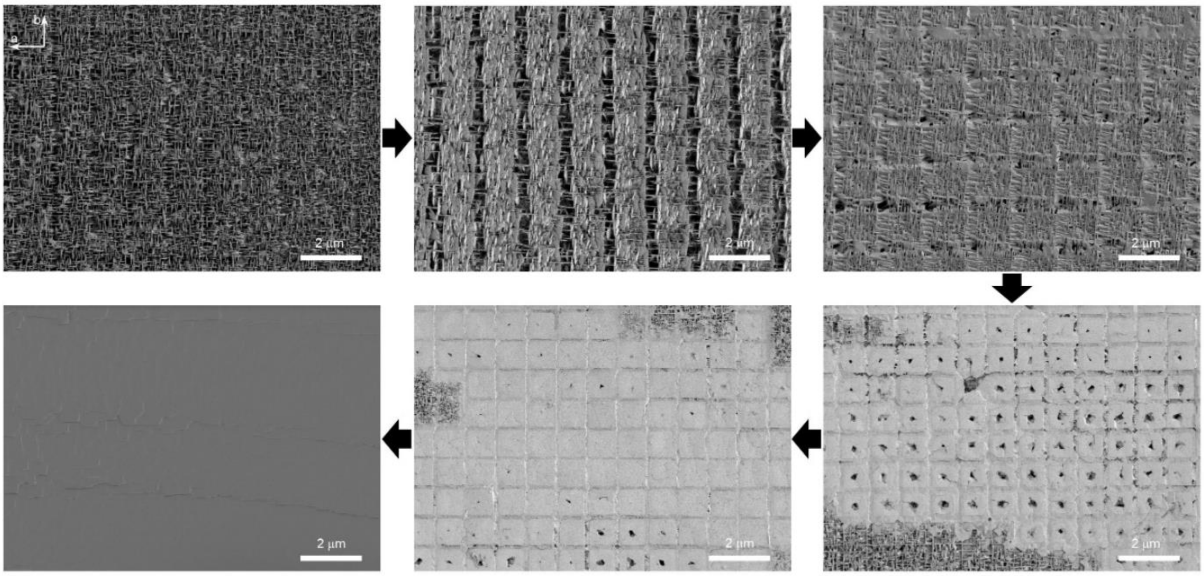

**Supplementary Fig. 2 | Detailed merging processes of epitaxial low-dimensional perovskites.** SEM images clearly show that the initial crisscross crystals gradually expand and contact each other to form a completely merged thin film.

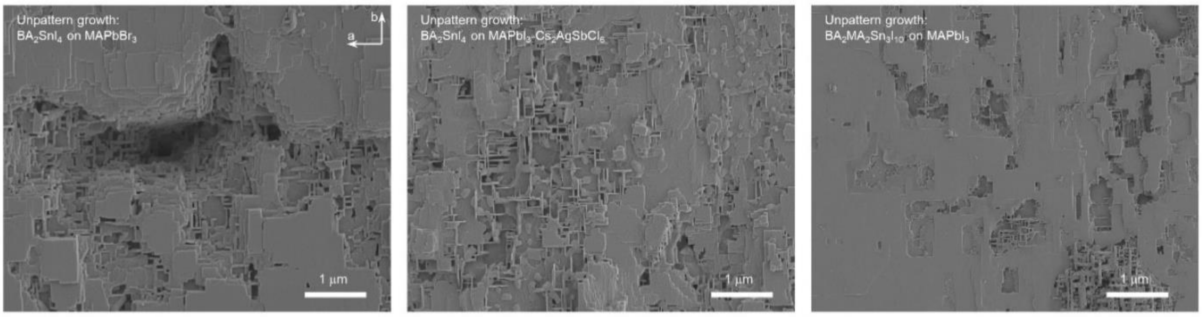

**Supplementary Fig. 3 | Epitaxial growth of low-dimensional perovskites on different 3D perovskite substrates.** Similar crisscross crystal morphology can be observed.

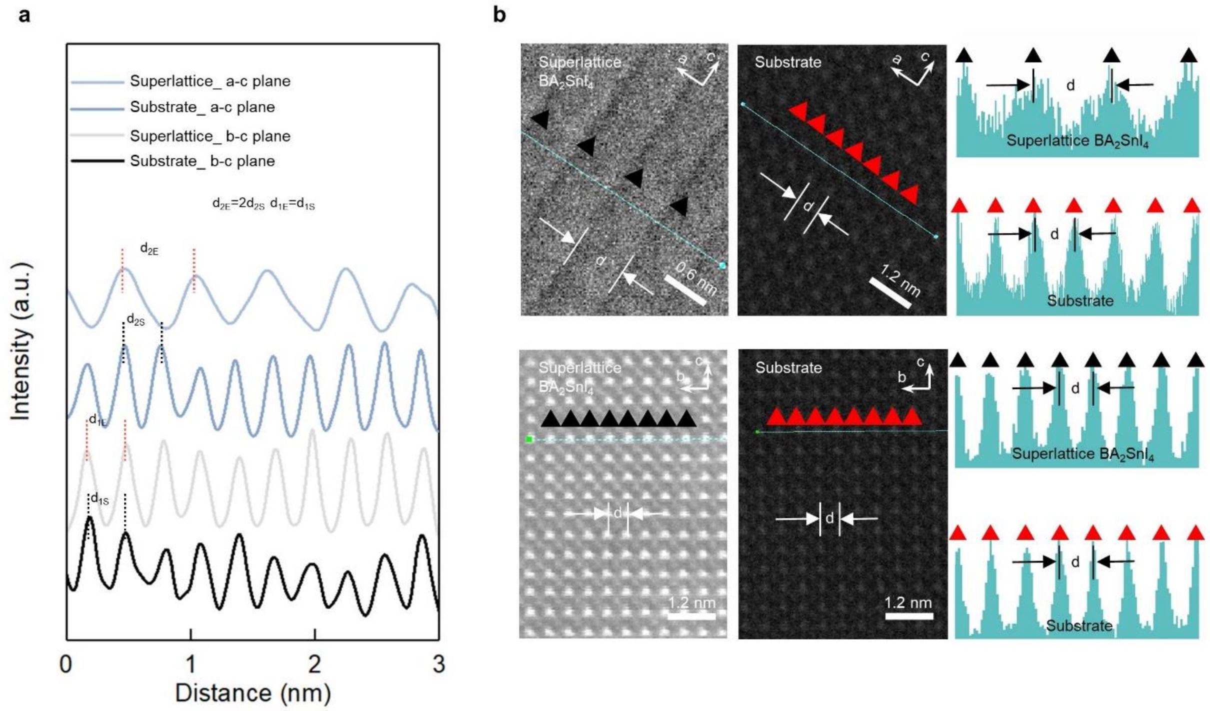

**Supplementary Fig. 4 | Mapping of the *d*-spacing.** (**a**) The extracted linear *d*-spacing curves from Fig. 1B. Along the *b* direction, the *d*-spacing of the epitaxial layer equals that of the substrate. However, along the *a* direction, the *d*-spacing of the epitaxial layer is two times that of the substrate. (**b**) Detailed *d*-spacing mapping from both *a*-*c* and *b*-*c* planes. In the *b* direction, the lattice constant of the Sn-I slab (~6.04 Å when conventionally grown, as calculated from x-ray diffraction) is ~5.96 Å, yielding 1.32 % strain. In the *a* direction, the *d*-spacing is ~11.92 Å, containing one Sn-I slab (~6.04 Å when conventionally grown) and one organic spacer (~7.00 Å when conventionally grown, as calculated from x-ray diffraction), corresponding to an overall compressive strain of 8.59%, which matches to the XRD results perfectly [22].

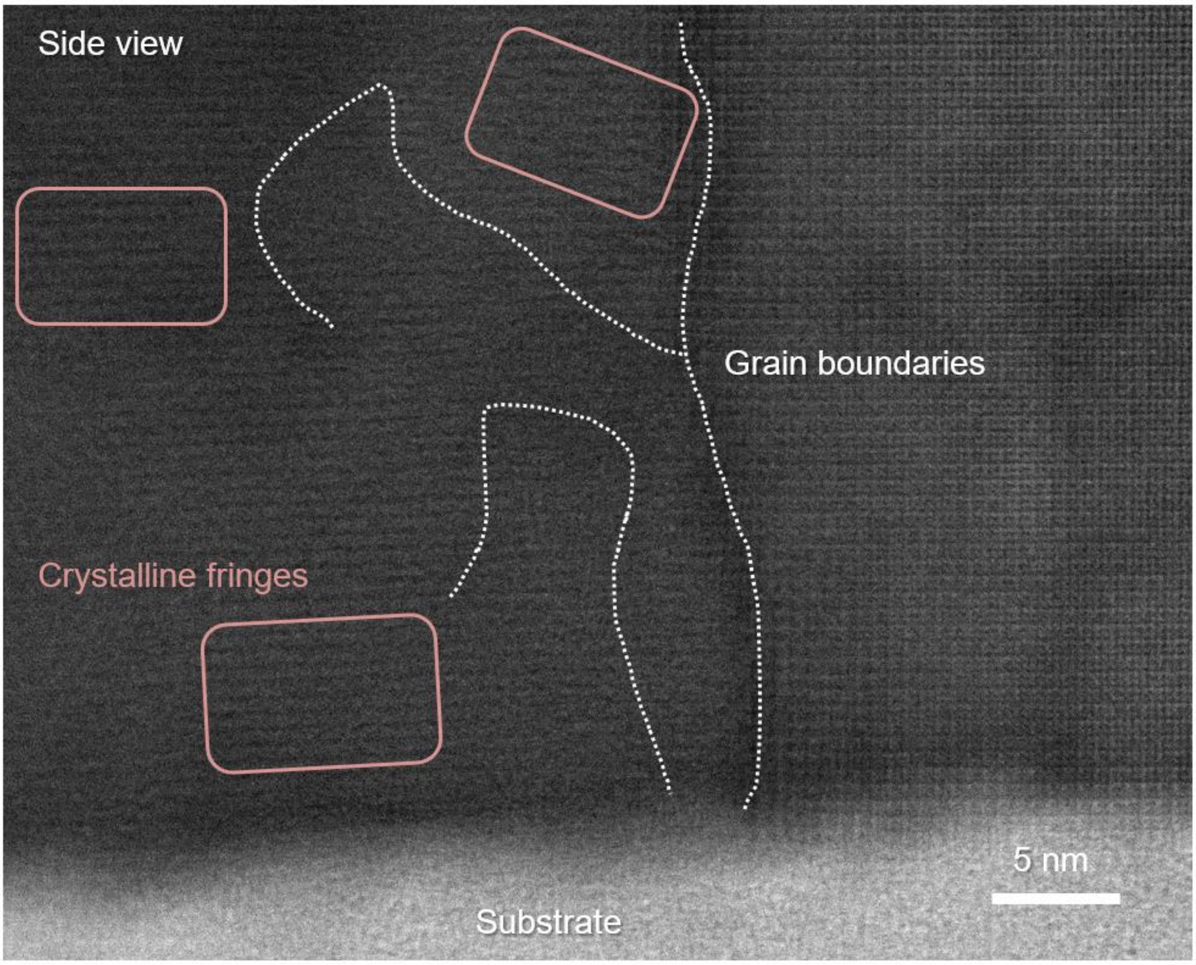

**Supplementary Fig. 5 | Cross-sectional high-resolution STEM image of a polycrystalline film.** It is clear to see that grain misorientations and boundaries exist along the thin-film thickness direction, indicating strong barriers for carrier transport in common devices with top and bottom contacts.

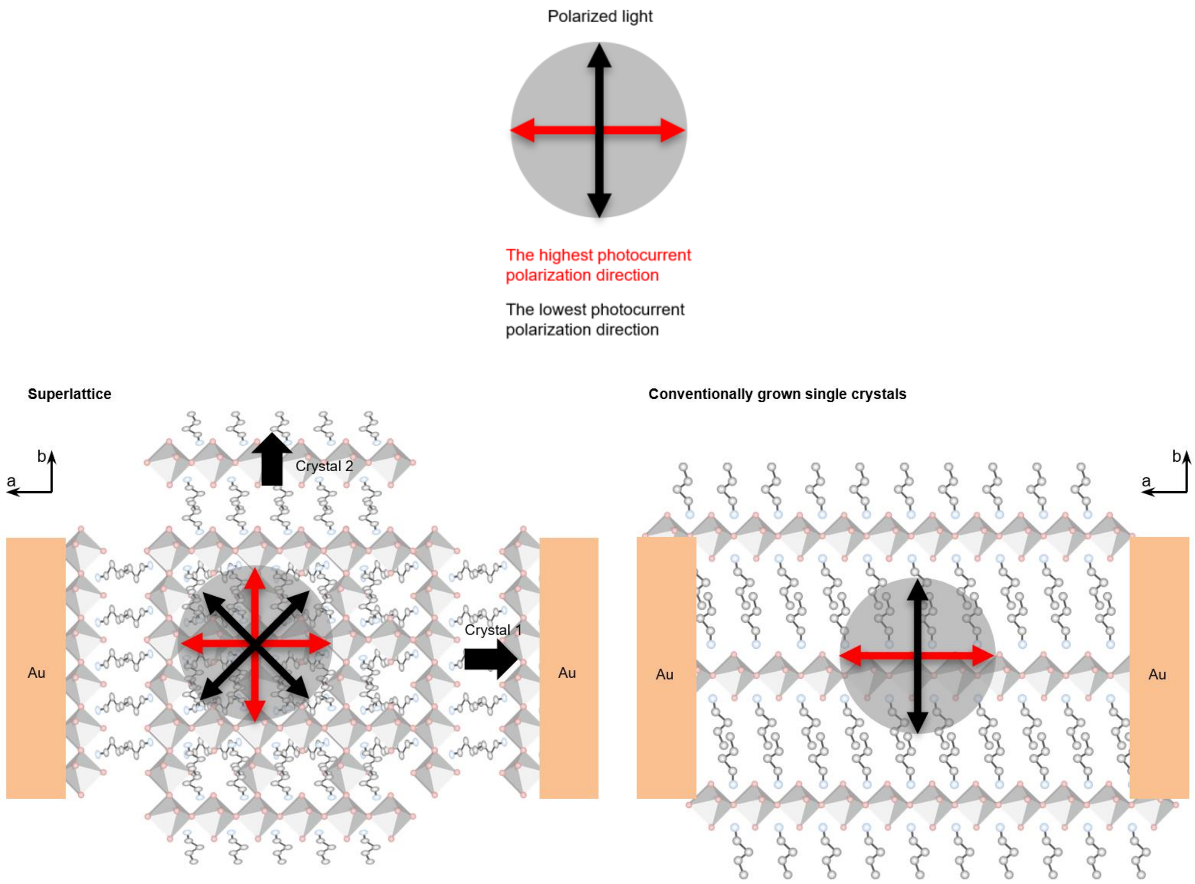

**Supplementary Fig. 6 | Schematics of the polarized photocurrent measurement.** The as-formed superlattice film contains a matrix-like structure, with two perpendicular crystals in two different orientations, corresponding to a 90° period for the polarized photocurrent. In contrast, the conventionally grown single crystal shows a 180° period due to its typical two-dimensional orientation.

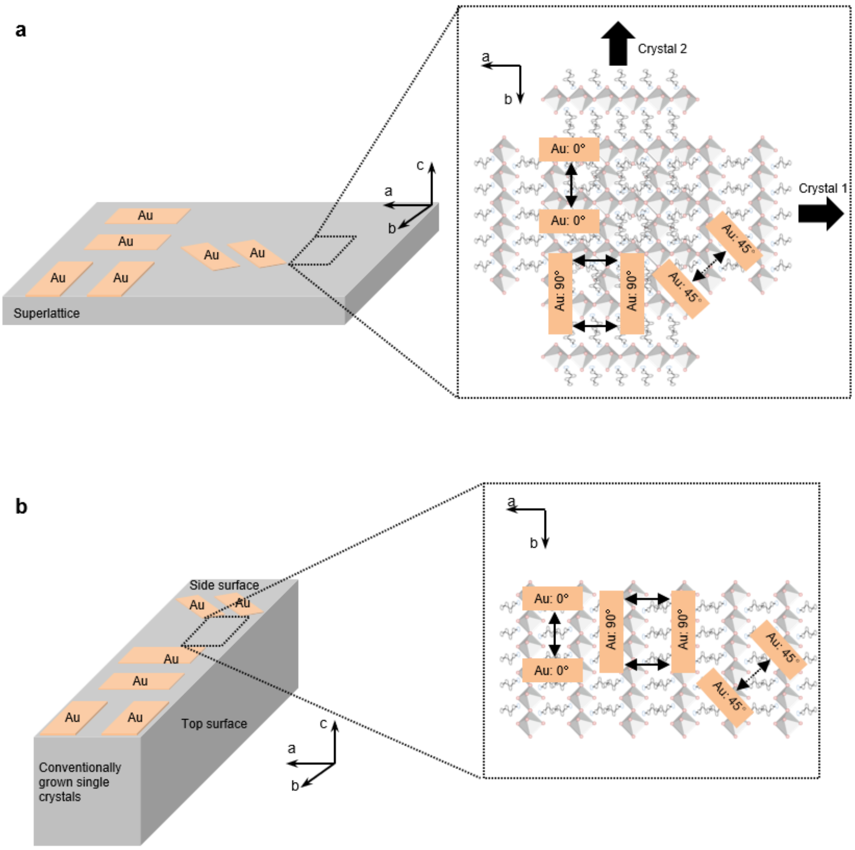

**Supplementary Fig. 7 | Schematics of the orientation-dependent transient photovoltage measurements.** (**a**) The schematic shows three Au electrode pairs on top of an epitaxial low-dimensional perovskite layer. The 0° and 90° are considered to be the same because the superlattice is formed by two perpendicular crystal plates, which exhibit a relatively long carrier lifetime. The 45° experiences organic barriers, leading to a relatively small carrier lifetime. (**b**) The schematic shows three Au electrode pairs on the side surface of a conventionally grown low-dimensional perovskite single crystal. The conventionally grown single crystals are relatively thin due to their intrinsic 2D characteristics. Therefore, a long-time is needed to grow such crystals so that the *a*-direction is thick enough for depositing electrodes on the side surface. The 0° exhibits the longest carrier lifetime due to the absence of organic barriers. In contrast, the 90° exhibits the lowest carrier lifetime, while the 45° condition shows a lifetime in between.

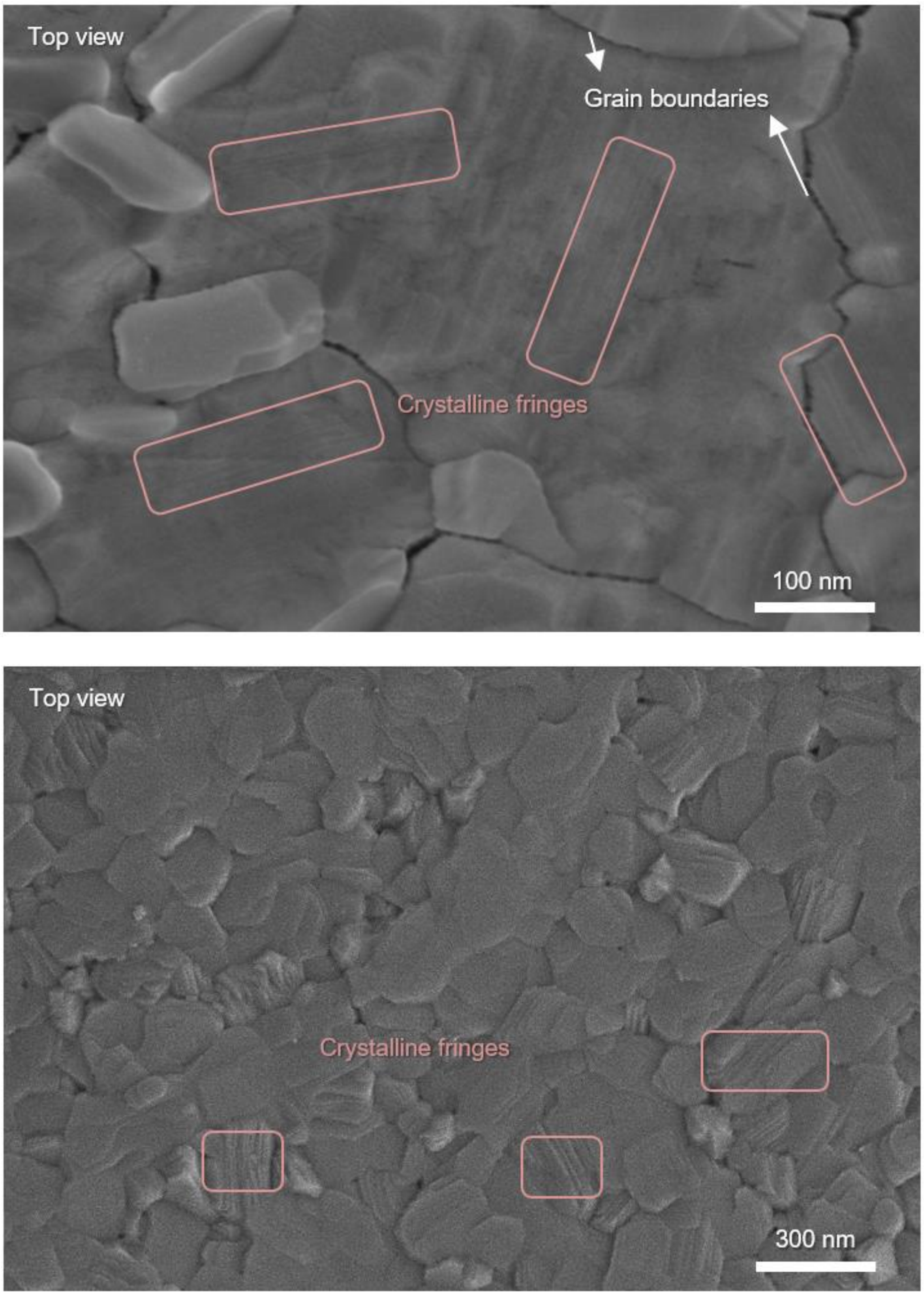

**Supplementary Fig. 8 | SEM images of polycrystalline thin films.** Grain misorientations and boundaries are numerous, suggesting strong energy barriers in every direction.

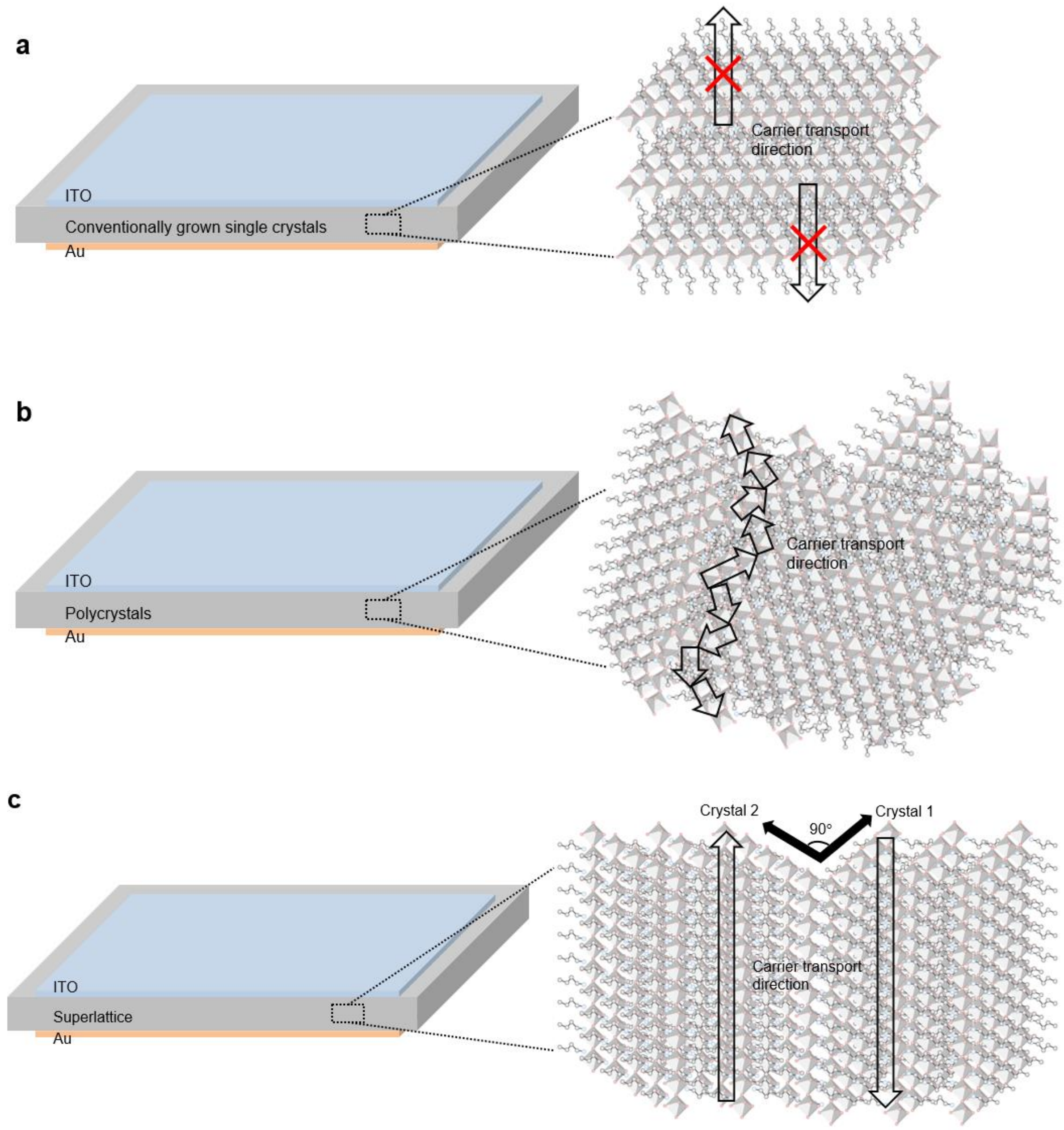

**Supplementary Fig. 9 | Schematics of the transient photocurrent measurements of three device structures.** (**a**) The conventionally grown single crystal has all organic spacers in the carrier transport direction, indicating the strongest energy barriers. (**b**) The polycrystals contain randomly orientated grains, where the organic spacers and the grain boundaries are isotropically distributed, suggesting strong energy barriers. (**c**) The epitaxial superlattice has no organic spacer in the carrier transport path, indicating negligible energy barriers.

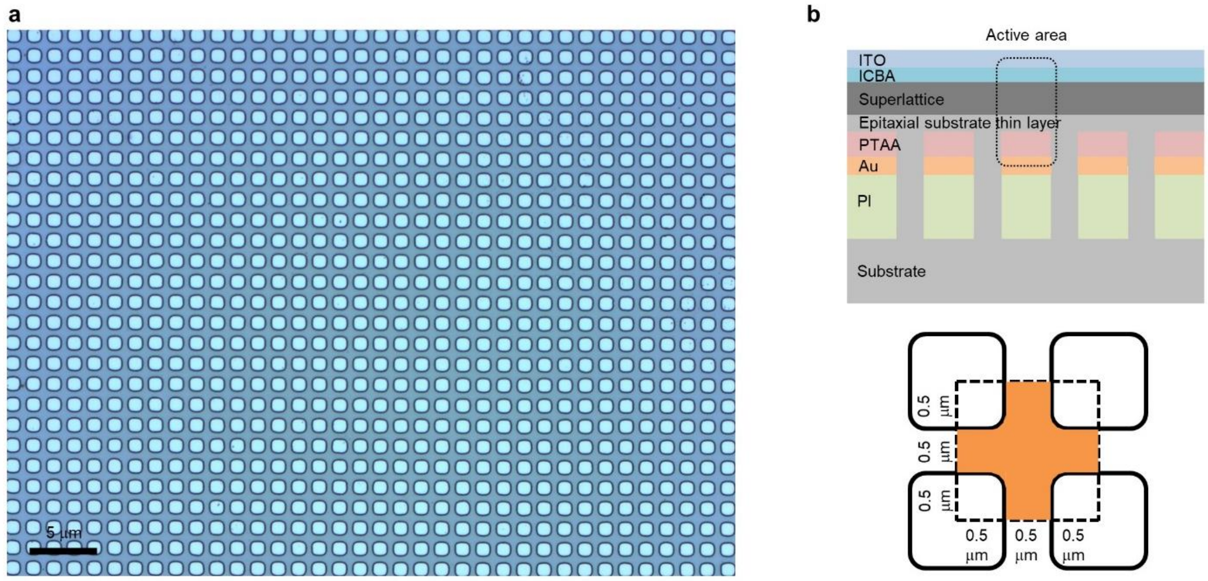

**Supplementary Fig. 10 | The configuration of *in-situ* fabricated devices.** (**a**) An optical image of the pre-patterned polyimide mask with deposited Au and PTAA layers. (**b**) The schematic cross-section of the device. A pre-pattern polyimide (PI) is deposited with layers of Au and PTAA and used as the growth mask and the bottom contact. A thin epitaxial layer of substrate is grown first to facilitate the growth of strained low-dimensional perovskite superlattice. The top and bottom electrodes do not have the same size, where the calculated active area between the top and bottom electrodes is around 55% of the entire area, which sacrifices the calculated power conversion efficiency.

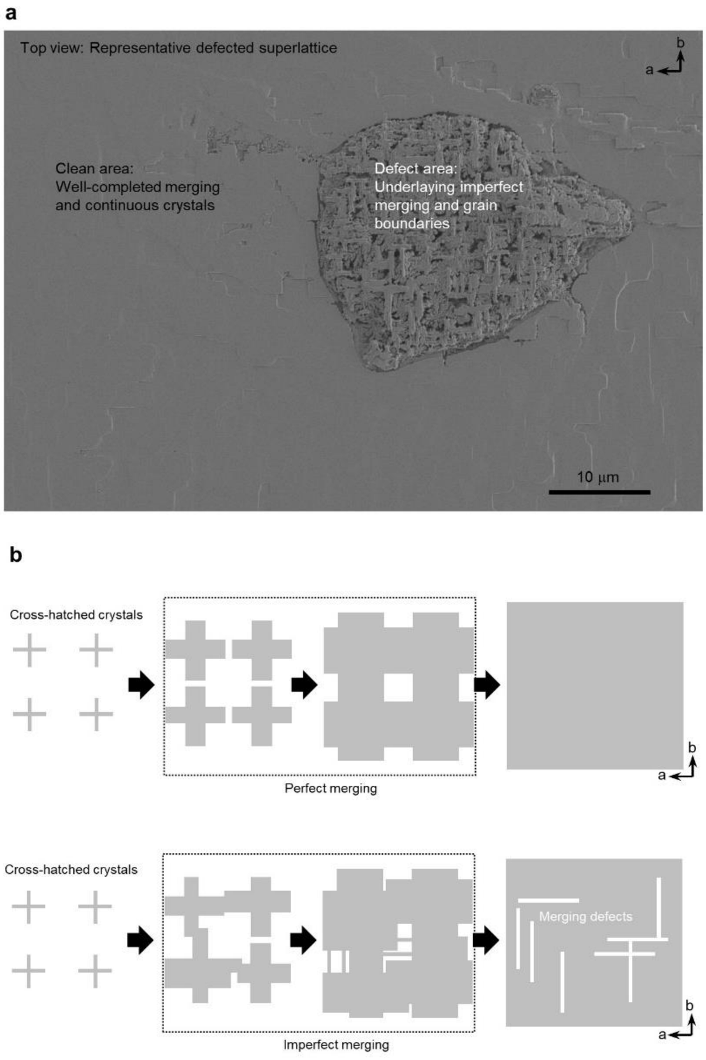

**Supplementary Fig. 11 | Imperfect merging in the superlattice.** (**a**) An SEM image of a superlattice that is intentionally broken to investigate the merging process. The merged film, albeit with a flat surface, may still bury invisible crystal boundaries. Structural defects are from the imperfect crystal merging because of the large lattice mismatch between the substrate and the organic spacer in the epitaxial layer. (**b**) Schematics showing the merging process with those crisscross thin crystal plates. The perfect merging, which requires the lattice orientation matching in both *a* and *b* directions, is impractical due to the existence of both organic spacers and inorganic slabs. The lattice misorientation between the organic spacers and inorganic slabs is impossible to avoid, resulting in merging defects.

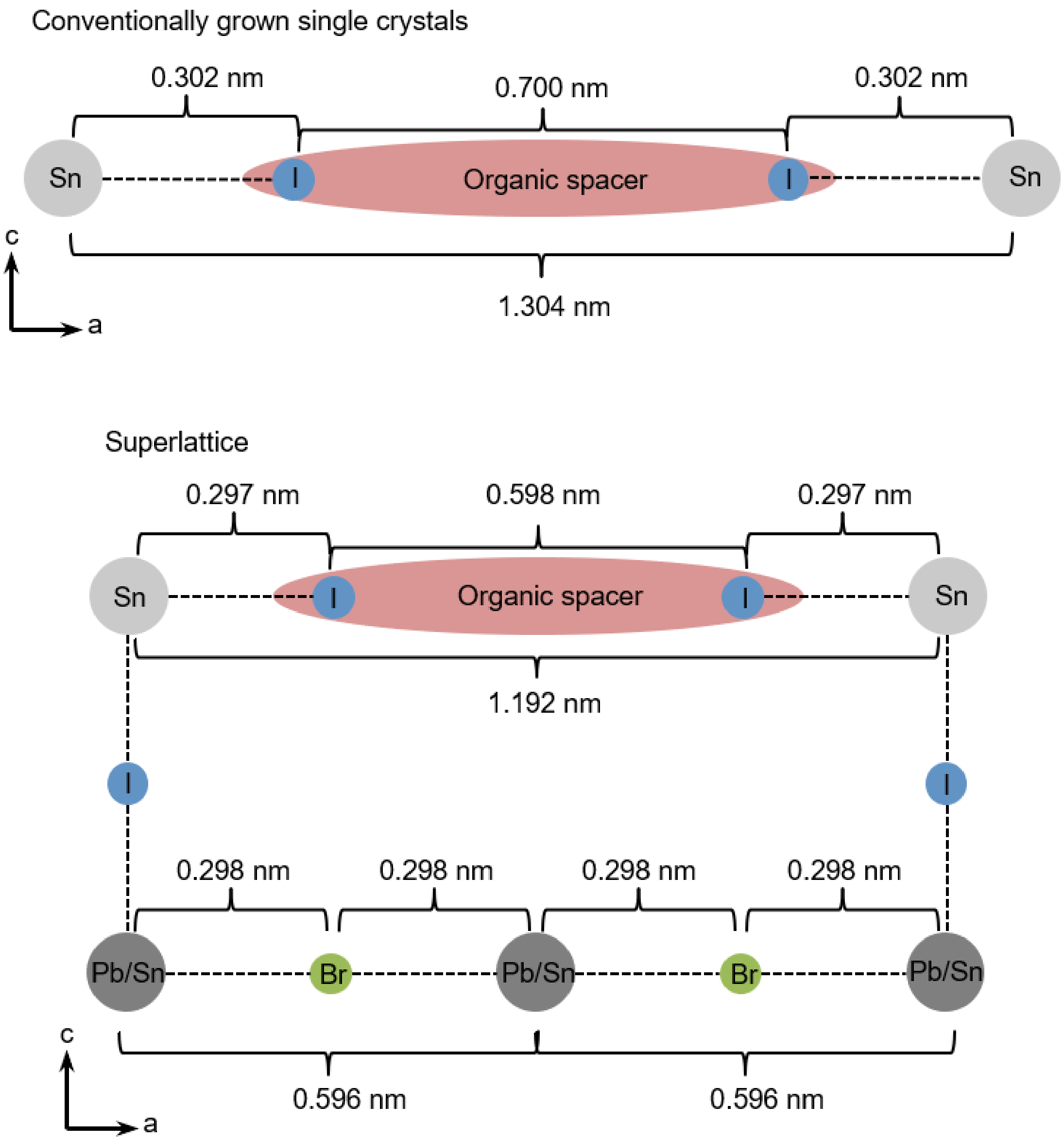

**Supplementary Fig. 12 | Schematic models of the epitaxial lattice strain.** Computational results show the lattice parameters from optimized stable crystal structures. In the conventionally grown Ruddlesden-Popper structure, the length of the Sn-I bond adjacent to the organic spacer is ~0.302 nm, and the distance between two I atoms is ~0.700 nm, which contains one organic spacer. In the superlattice case, the length of the Sn-I bond adjacent to the organic spacer is ~0.297 nm, and the distance between two I atoms is ~0.598 nm, which contains one organic spacer. The substrate has a Pb/Sn-Br bond of ~0.298 nm. Due to the epitaxy, the superlattice is not the Ruddlesden-Popper structure anymore.

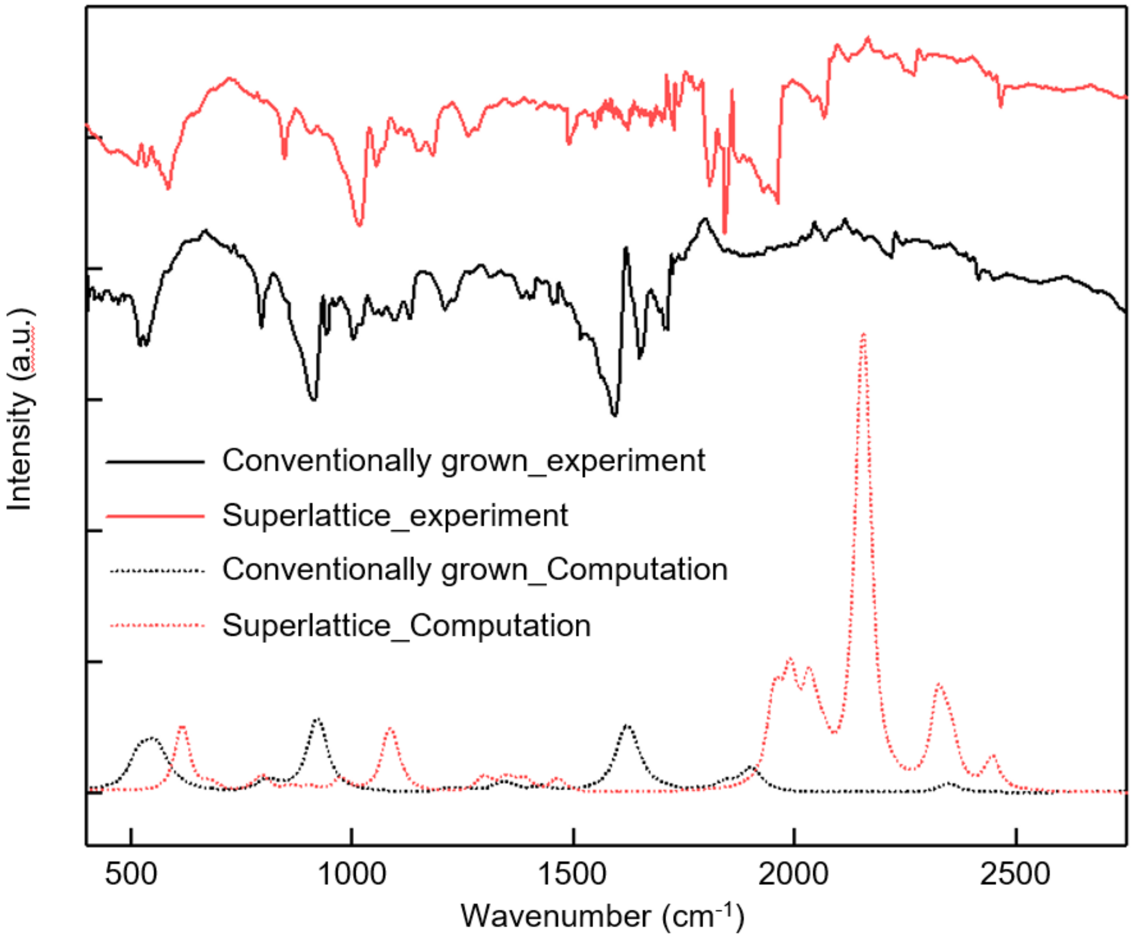

**Supplementary Fig. 13 | Fourier-transform infrared spectroscopy characterizations.** Both superlattice and conventionally grown single crystals have been characterized. The results show that the peaks in the superlattice shift apparently to higher wavenumbers, indicating the vibration frequencies of the organic bonds in the superlattice are enhanced, which is from the compressed organic spacers in the superlattice. To verify the observations, the Fourier-transform infrared spectroscopy has been simulated by only tunning the organic spacer from the original (conventionally grown) to the compressed (superlattice) states. In the computational results, the as-modeled superlattice exhibits clear peak shifting to higher wavenumbers than the conventionally grown structure, which is similar to the experimental measurements, confirming that the compressed bonds in the organic spacer of the superlattice are the reason for the enhanced vibration frequency.

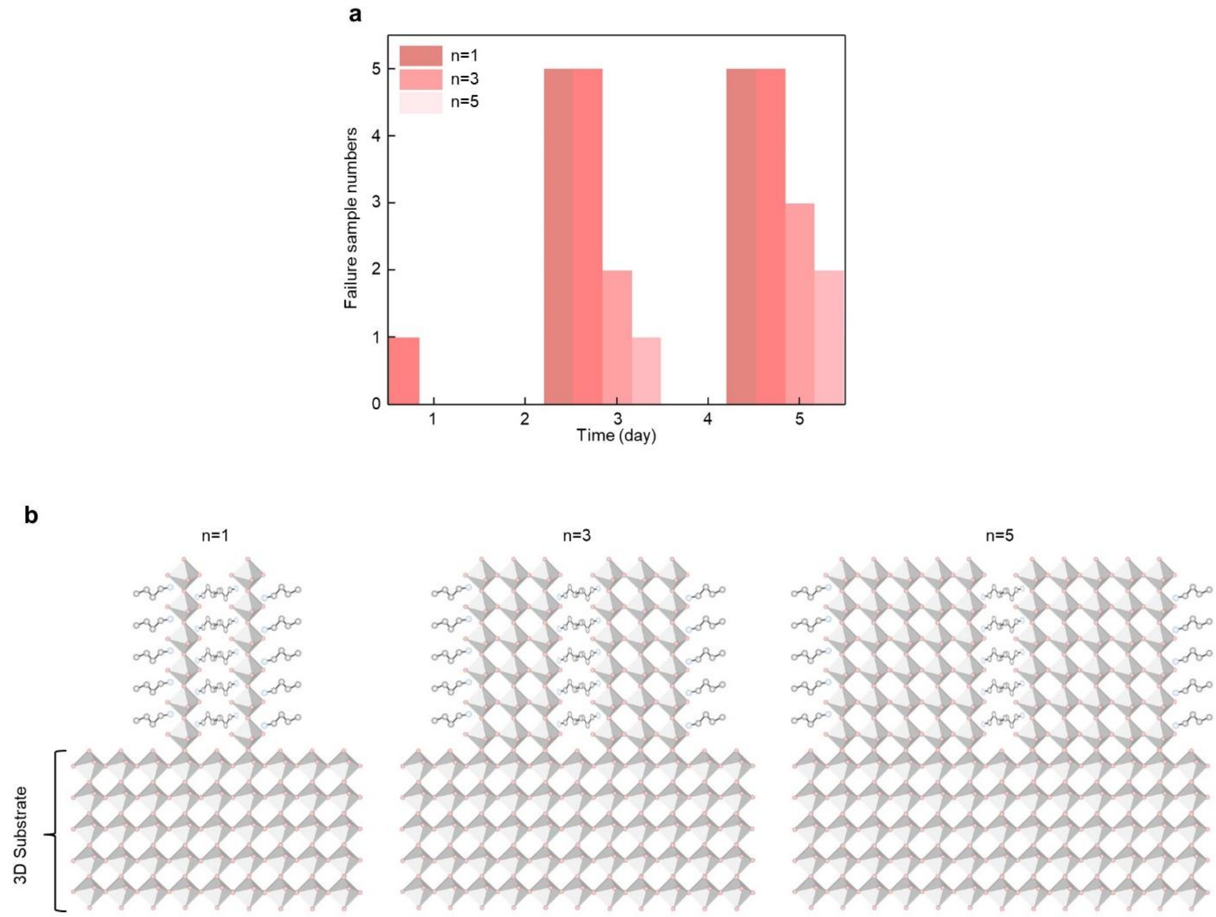

**Supplementary Fig. 14 | A summary of degradation of superlattices with different *n*-values.** (**a**) The degradation of superlattices is found to be highly related to the *n*-values. A higher *n*-value exhibits higher stability. (**b**) Schematics show the epitaxial superlattices with different *n*-values. If the volume ratio of the inorganic slabs is higher, the inorganic slabs are more resistant to the lattice strain applied from the compressed organic spacers.

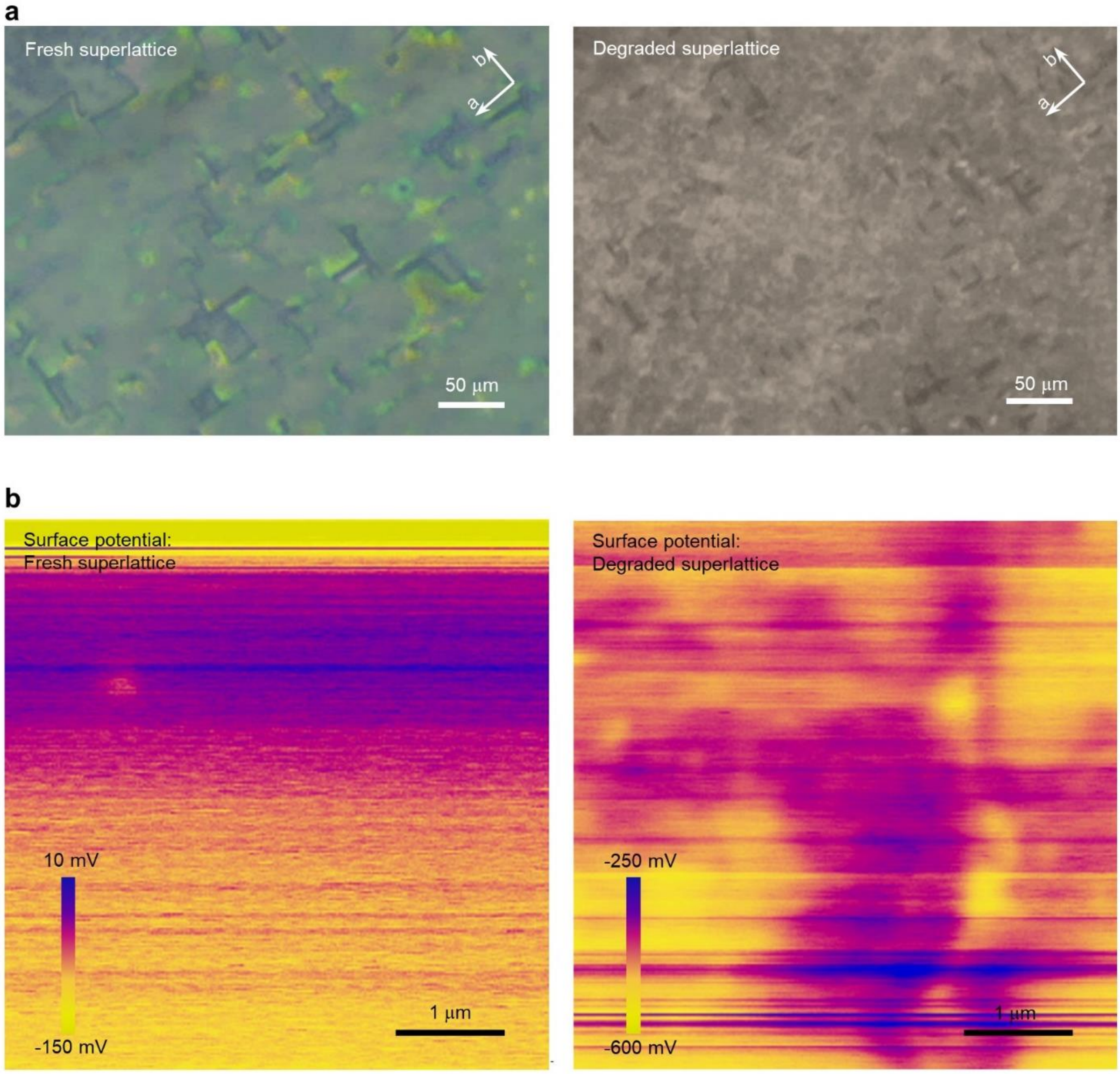

**Supplementary Fig. 15 | Degradation in the superlattice.** (**a**) Optical images show clear changes in the morphology and color from the fresh to the degraded superlattices, where the degraded samples show obviously amorphous structures. (**b**) Kelvin probe force microscopy measurements confirm that the work function decreases enormously in the degraded sample, suggesting more insulating properties. Additionally, the larger variations in the measured voltages of the degraded sample than those of the fresh sample also indicate that the surface uniformity has been largely damaged by the degradation.

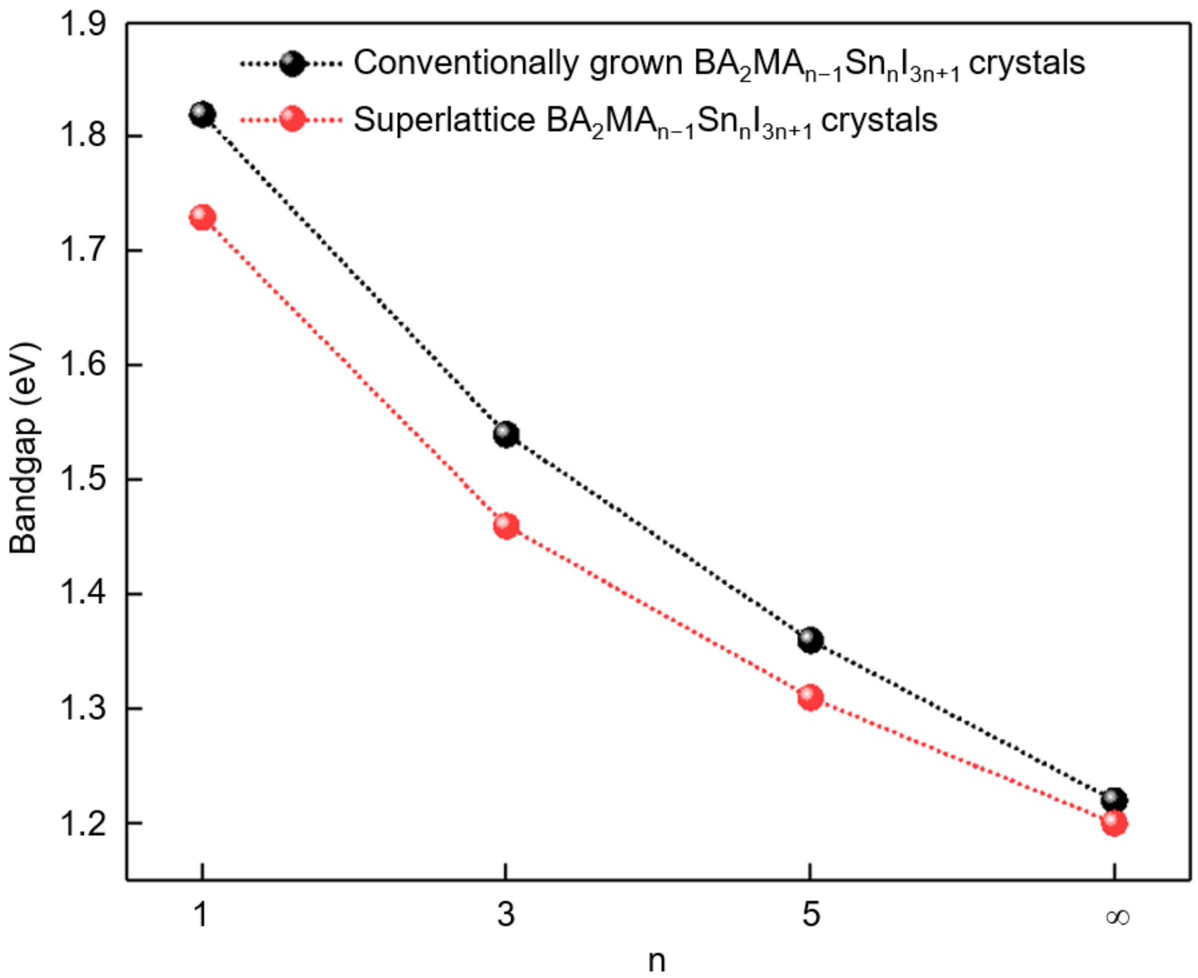

**Supplementary Fig. 16 | A summary of bandgaps for conventionally grown and superlattice low-dimensional Sn perovskites.** Those values are from UV-Vis measurements under the reflection mode. The superlattices generally exhibit a smaller bandgap than the conventionally grown single crystals. As *n* increases, the bandgap also becomes smaller due to the reduced quantum confinement from the organic spacers. An extreme case is that when *n* equals to infinity, the low-dimensional perovskites become 3D perovskites.

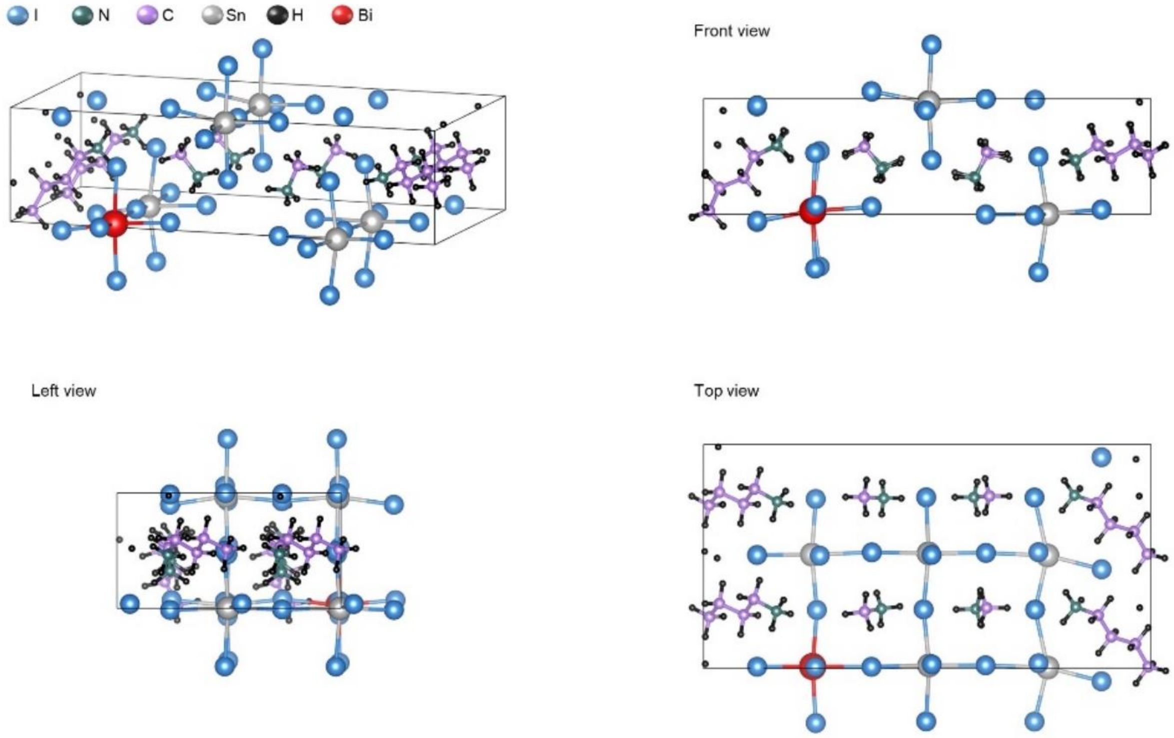

**Supplementary Fig. 17 | The unit cell of the $BA_2MA_2Sn_3I_{10}$ ($n$ = 3) superlattice.** One unit cell has been modeled to represent the overall structure due to the limited computational power available. Because only six $Sn^{2+}$ ions are included in the modeling, the minimal $Bi^{3+}$ percentage in the alloyed unit cell is 16.7%, which results from the replacement of one $Sn^{2+}$ ion from the original six $Sn^{2+}$ ions.

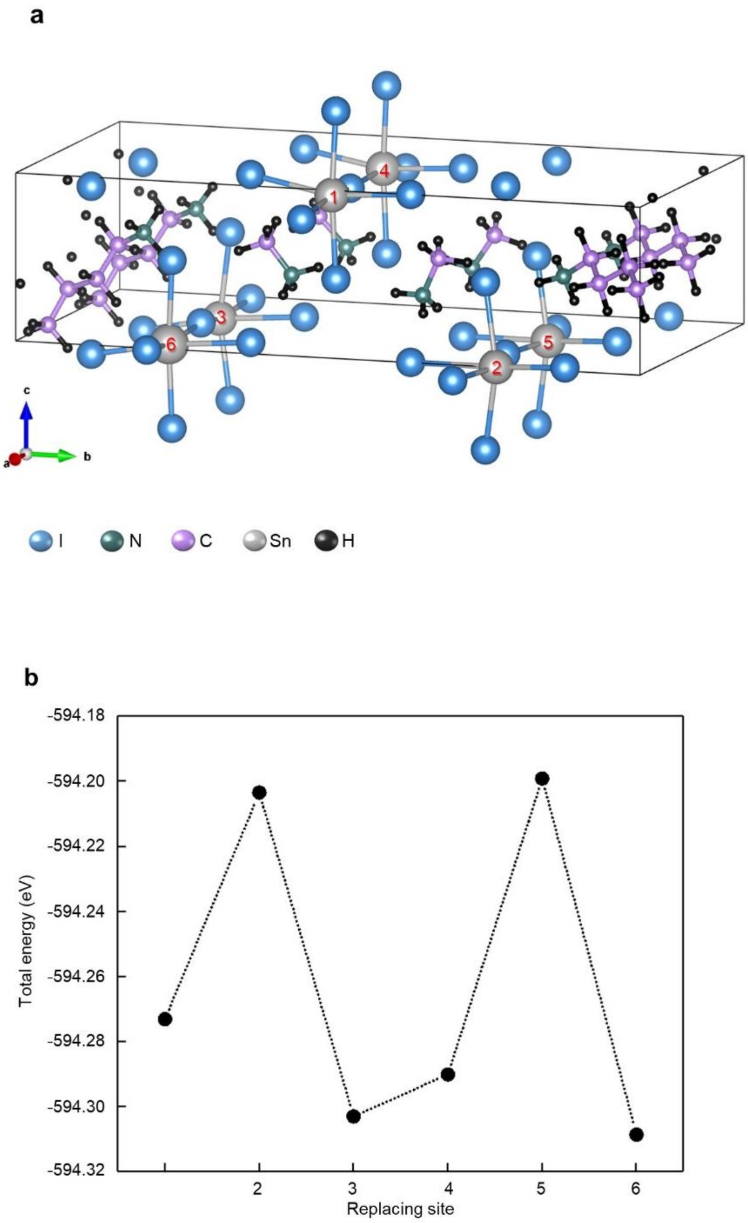

**Supplementary Fig. 18 | Total energy calculations with $Bi^{3+}$ alloying.** (**a**) The unit cell structure for the $BA_2MA_2Sn_3I_{10}$ superlattice before $Bi^{3+}$ alloying. To simplify the modeling, the lattice strain from the organic spacers is only applied from the left side. Sn atoms at different sites are marked with numbers from 1 to 6, which are replaced by the $Bi^{3+}$ to form six different structures. (**b**) The total energy with the different sites (from 1 to 6) of $Sn^{2+}$ will be replaced by $Bi^{3+}$. When the $Bi^{3+}$ is set to be at sites 3 or 6, the unit cell exhibits the smallest total energy, indicating the most stable structure.

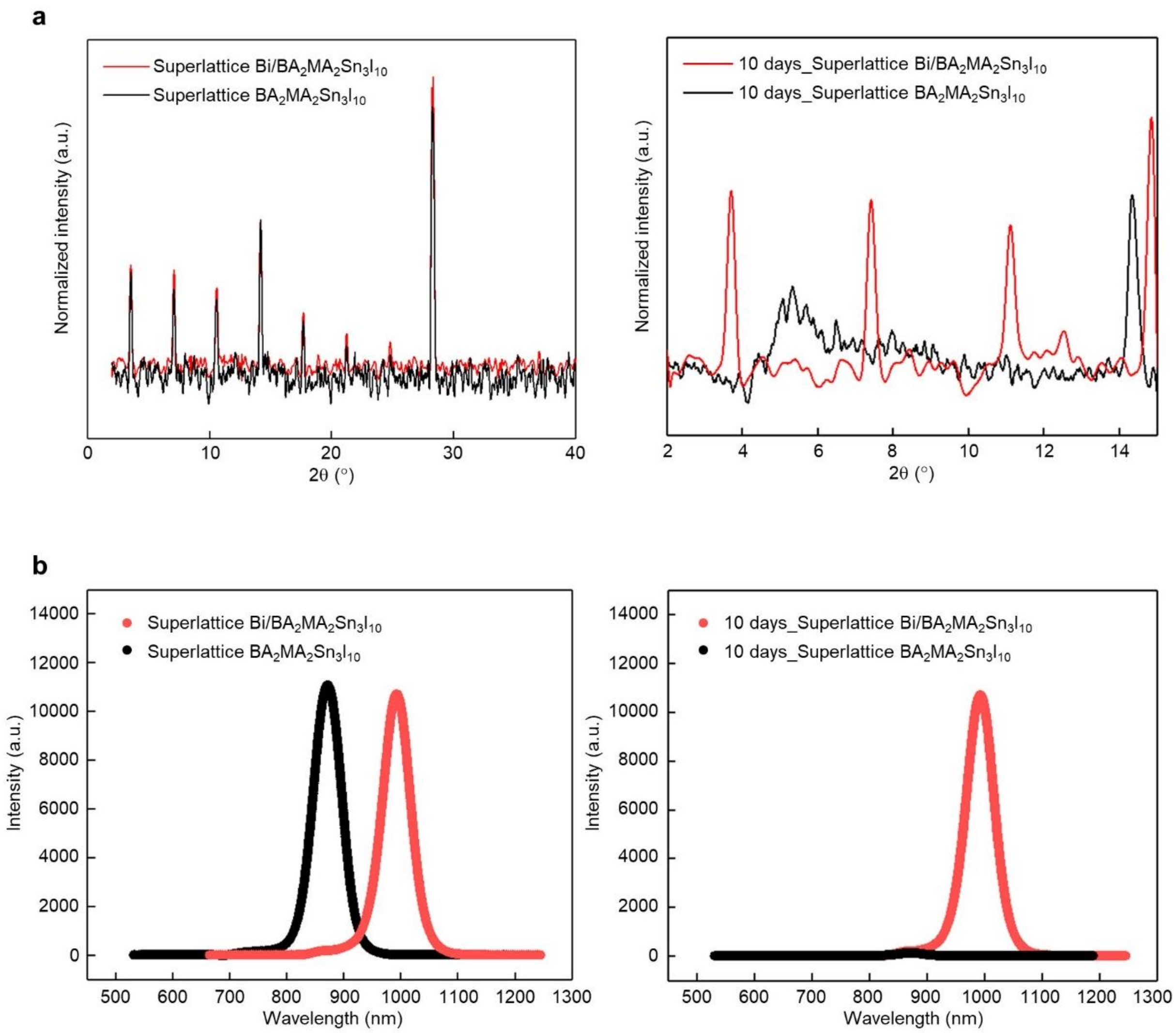

**Supplementary Fig. 19 | XRD and PL characterizations of the Bi$^{3+}$ alloyed superlattice in Fig. S17.** (**a**) XRD results show that there is no noticeable peak shifting after 10% Bi$^{3+}$ alloying, and the superlattice structure also does not change because it is anchored by the substrate (left). After 10 days, the structure of the Bi$^{3+}$ alloyed superlattices is still stable, but the structure of the Bi$^{3+}$-free superlattices degrade obviously (right). (**b**) PL results show that the Bi$^{3+}$ alloying decreases the bandgap (left), and no noticeable PL intensity change is found after 10 days (right).

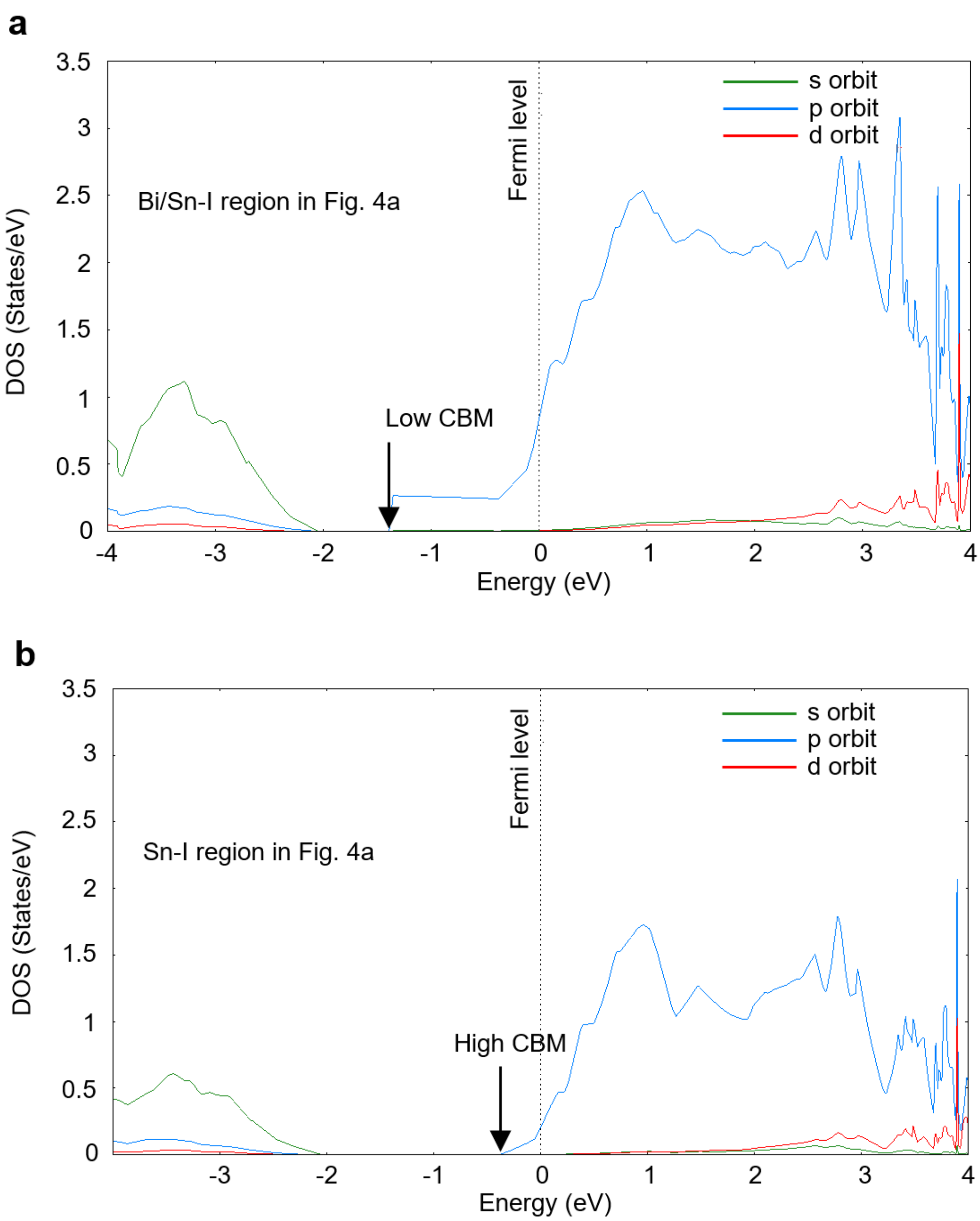

**Supplementary Fig. 20 | Calculated electronic structures of the $Bi^{3+}$ alloyed $BA_2MA_2Sn_3I_{10}$ superlattice.** $Bi^{3+}$ alloying vastly decreases the CBM position, resulting in a smaller bandgap. (**a**) The density of states (DOS) plot of the Bi/Sn-I region in Fig. 4A. (**b**) The DOS plot of the Sn-I region in Fig. 4A. The CBM position in (**a**) has been noticeably decreased compared with the case in (**b**), indicating that Bi/Sn-I region exhibits a smaller bandgap, which is mainly because of the energy contribution from the p orbitals of the $Bi^{3+}$ ions.

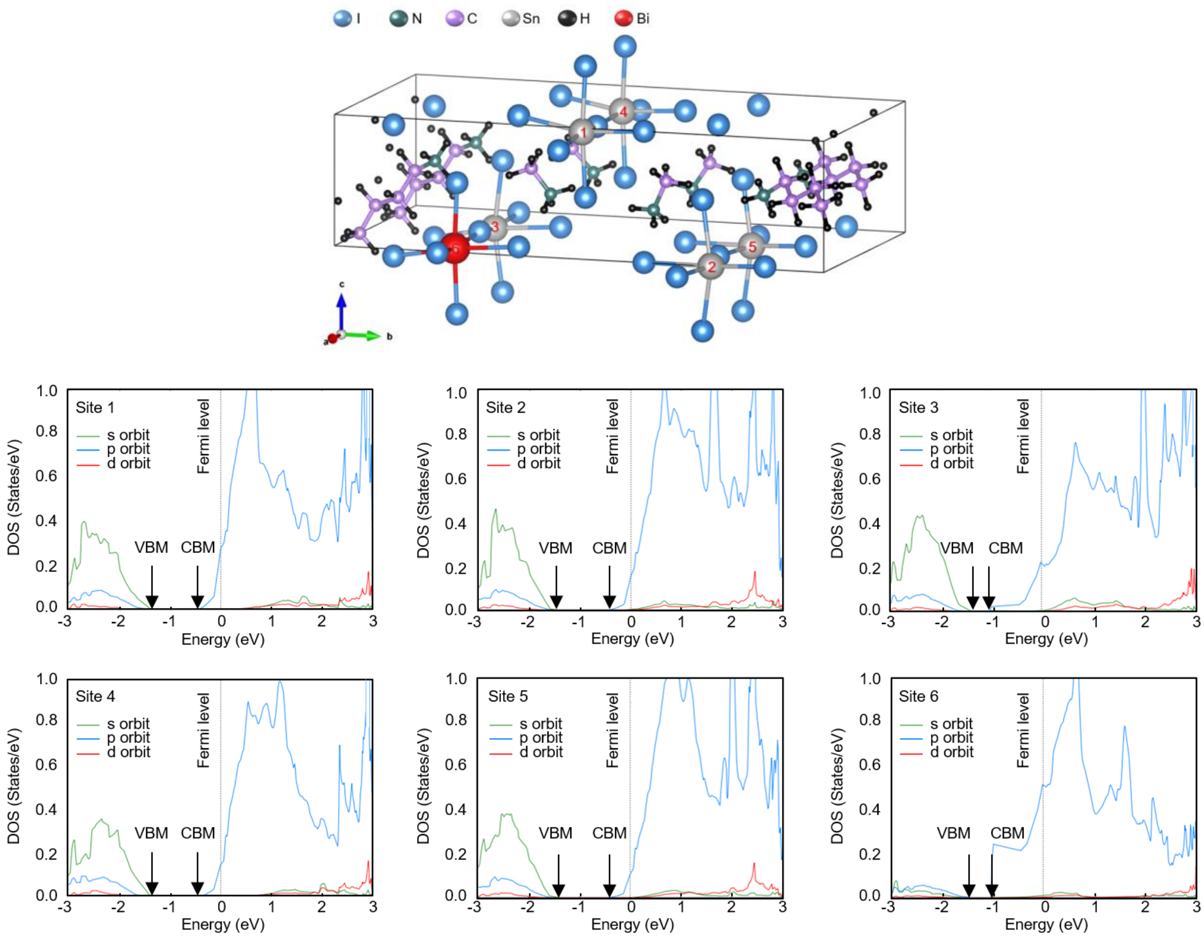

**Supplementary Fig. 21 | Calculated electronic structures of the $BA_2MA_2Sn_3I_{10}$ superlattice when $Bi^{3+}$ replaces $Sn^{2+}$ at different sites.** The $Bi^{3+}$ could influence the electronic structure of surrounding $Sn^{2+}$ by replacing the original Sn-I-Sn structure with the Sn-I-Bi structure. The DOS plots of the six ions in the unit cell are shown. Those ions closer to the $Bi^{3+}$ have a smaller bandgap, which is caused by the decreased CBM position from the p orbitals of the $Bi^{3+}$ ions.

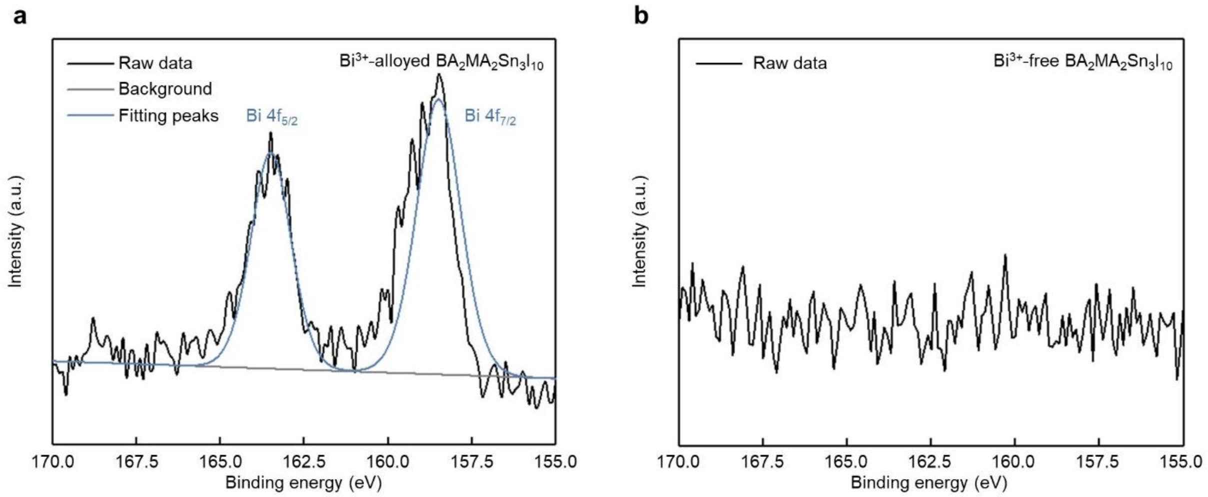

**Supplementary Fig. 22 | XPS measurements of Bi$^{3+}$ alloyed superlattice.** The successful alloying of Bi$^{3+}$ has been characterized by XPS measurements. Obvious peaks in (**a**) from the Bi 4f$_{5/2}$ and Bi 4f$_{7/2}$ are evident in the Bi$^{3+}$ alloyed $BA_2MA_2Sn_3I_{10}$ superlattice. However, the Bi$^{3+}$-free $BA_2MA_2Sn_3I_{10}$ superlattice in (**b**) does not have any noticeable peaks associated with the Bi.

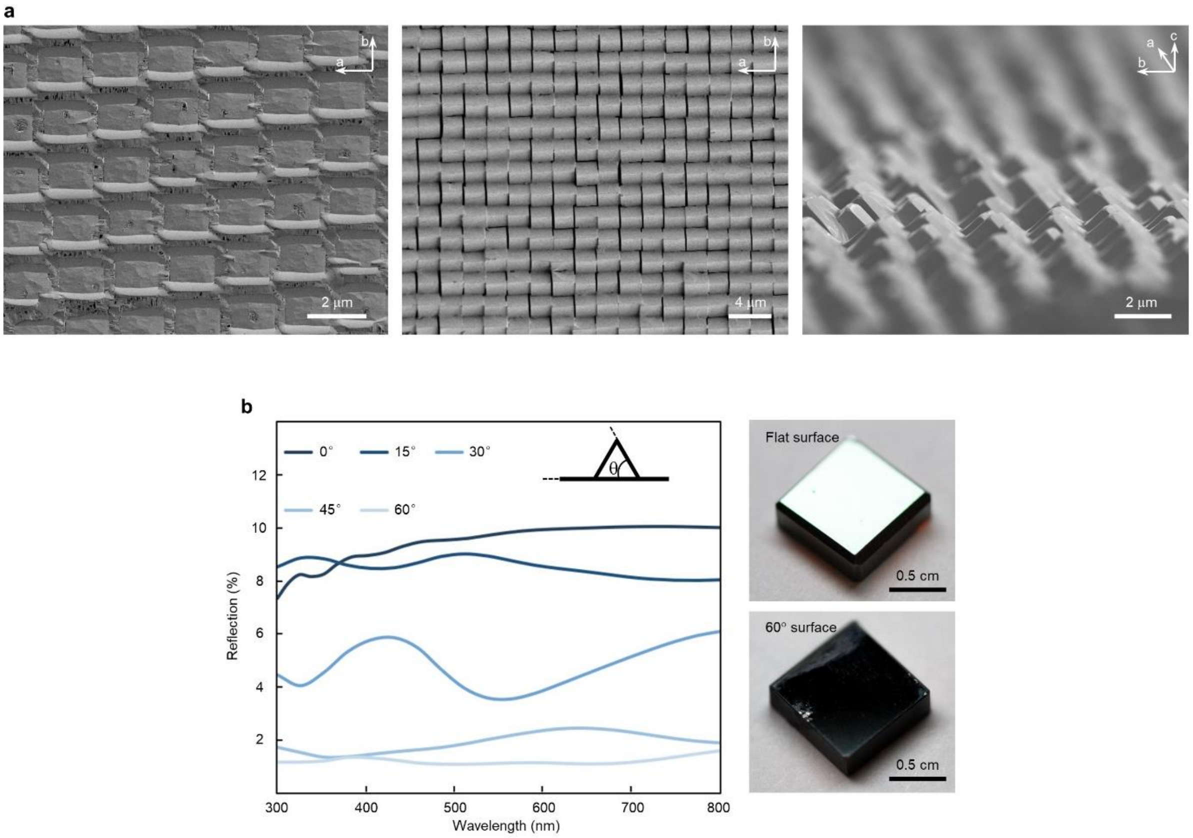

**Supplementary Fig. 23 | The textured surface and the light-trapping property of the superlattice.** (**a**) SEM images showing the textured surface of the epitaxial BA$_2$MA$_4$Sn$_5$I$_{16}$ layer grown on different crystal facets of the 3D perovskite substrate[15,28]. (**b**) Reflection measurement results show that the optimized tilting angle of the microstructures is 60°, which gives the smallest reflection, as evidenced by the optical images on the right.

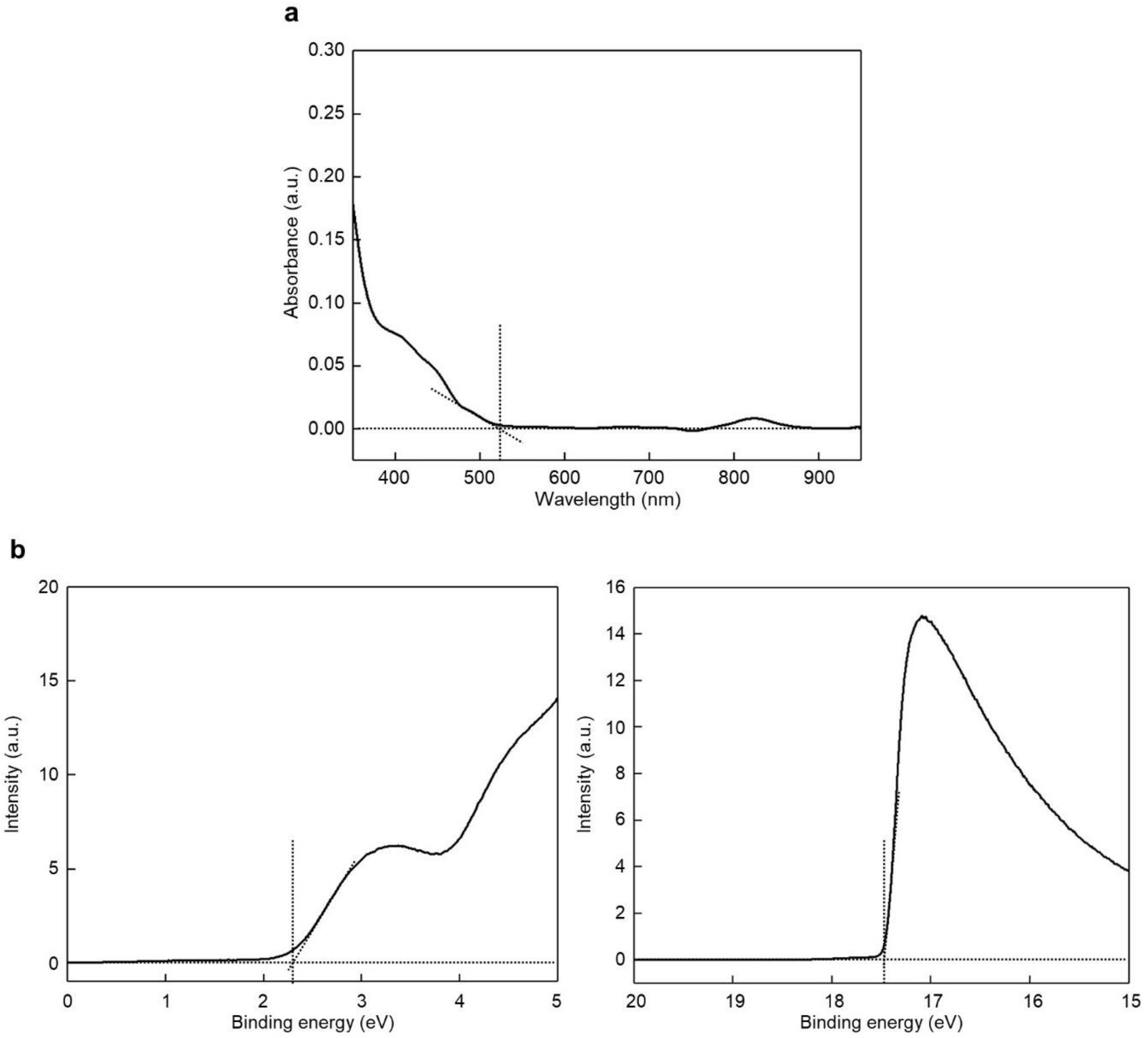

**Supplementary Fig. 24 | The band structure of the ICBA layer.** (**a**) UV-Vis measurements of the ICBA layer under the absorption mode. The bandgap is determined by the cutoff from the dash lines. (**b**) UPS measurements of the ICBA layer. The CBM is calculated by the cutoff from the dash lines in both high and low binding energy regions.

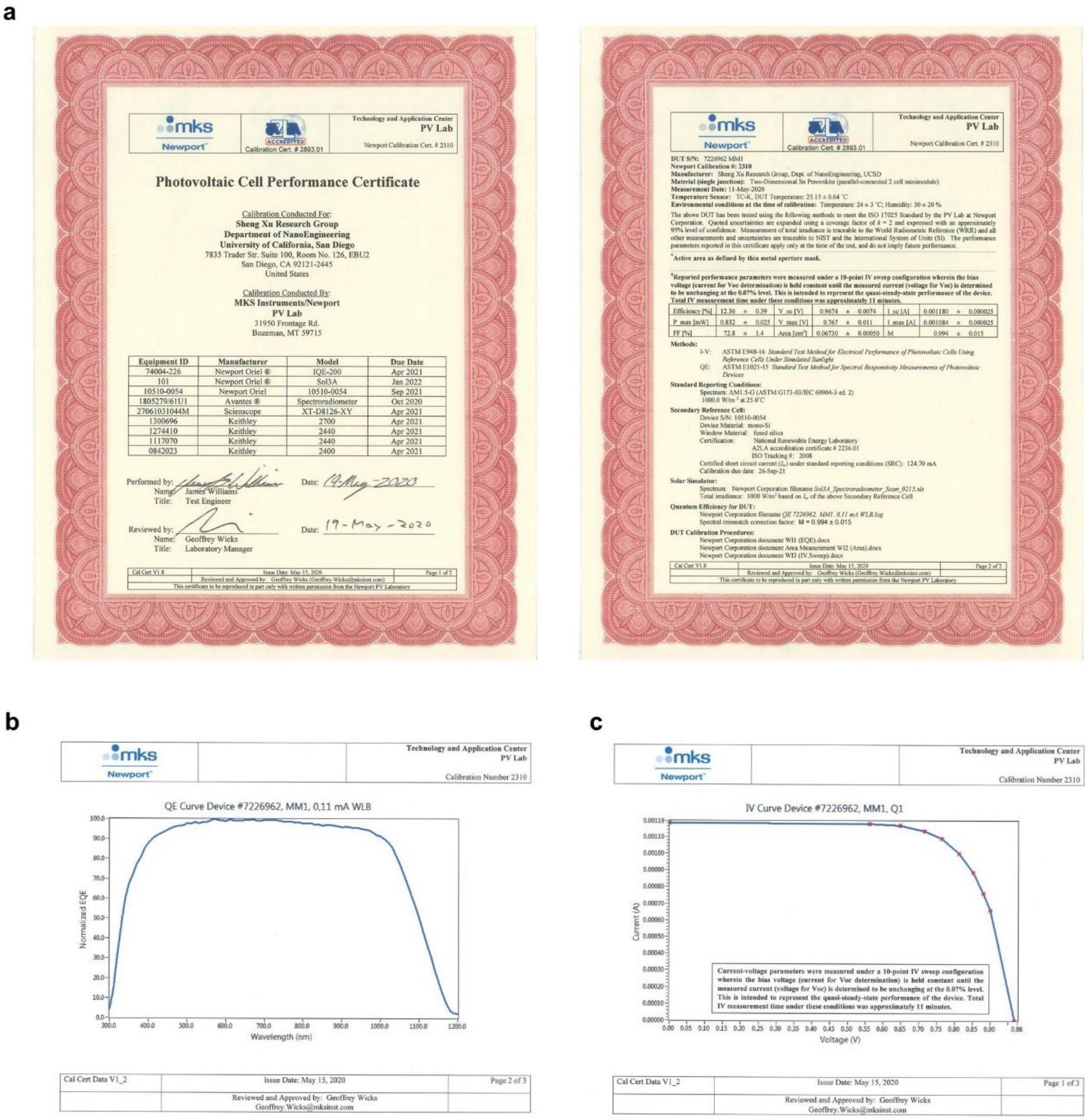

Technology and Application Center
PV Lab
Newport Calibration Cert. # 2310
Calibration Cert. # 2893.01

**Photovoltaic Cell Performance Certificate**

Calibration Conducted For:
**Sheng Xu Research Group**
**Department of NanoEngineering**
**University of California, San Diego**
7835 Trader Str. Suite 100, Room No. 126, EBU2
San Diego, CA 92121-2445
United States

Calibration Conducted By:
**MKS Instruments/Newport**
**PV Lab**
31950 Frontage Rd.
Bozeman, MT 59715

| Equipment ID | Manufacturer | Model | Due Date |
|---|---|---|---|
| 74004-226 | Newport Oriel ® | IQE-200 | Apr 2021 |
| 101 | Newport Oriel ® | Sol3A | Jan 2022 |
| 10510-0054 | Newport Oriel | 10510-0054 | Sep 2021 |
| 1805279/61U1 | Avantes ® | Spectroradiometer | Oct 2020 |
| 27061031044M | Sciencscope | XT-D8126-XY | Apr 2021 |
| 1300696 | Keithley | 2700 | Apr 2021 |
| 1274410 | Keithley | 2440 | Apr 2021 |
| 1117070 | Keithley | 2440 | Apr 2021 |
| 0842023 | Keithley | 2400 | Apr 2021 |

Performed by:
Name: James Williams
Title: Test Engineer
Date: 19-May-2020

Reviewed by:
Name: Geoffrey Wicks
Title: Laboratory Manager
Date: 19-May-2020

| | | |
|---|---|---|
| Cal Cert V1.8 | Issue Date: May 15, 2020 | Page 1 of 2 |
| | Reviewed and Approved by: Geoffrey Wicks (Geoffrey.Wicks@mksinst.com) | |
| This certificate to be reproduced in part only with written permission from the Newport PV Laboratory | | |

Technology and Application Center
PV Lab
Newport Calibration Cert. # 2310
Calibration Cert. # 2893.01

**DUT S/N:** 7226962 MM1
**Newport Calibration #: 2310**
**Manufacturer:** Sheng Xu Research Group, Dept. of NanoEngineering, UCSD
**Material (single junction):** Two-Dimensional Sn Perovskite (parallel-connected 2 cell minimodule)
**Measurement Date:** 11-May-2020
**Temperature Sensor:** TC-K, DUT Temperature: 25.15 ± 0.64 °C
**Environmental conditions at the time of calibration:** Temperature: 24 ± 3 °C; Humidity: 30 ± 20 %

The above DUT has been tested using the following methods to meet the ISO 17025 Standard by the PV Lab at Newport Corporation. Quoted uncertainties are expanded using a coverage factor of $k = 2$ and expressed with an approximately 95% level of confidence. Measurement of total irradiance is traceable to the World Radiometric Reference (WRR) and all other measurements and uncertainties are traceable to NIST and the International System of Units (SI). The performance parameters reported in this certificate apply only at the time of the test, and do not imply future performance.

***Active area as defined by thin metal aperture mask.**

**†Reported performance parameters were measured under a 10-point IV sweep configuration wherein the bias voltage (current for Voc determination) is held constant until the measured current (voltage for Voc) is determined to be unchanging at the 0.07% level. This is intended to represent the quasi-steady-state performance of the device. Total IV measurement time under these conditions was approximately 11 minutes.**

| | | | |
|---|---|---|---|
| Efficiency [%] | 12.36 ± 0.39 | V_oc [V] | 0.9674 ± 0.0074 |
| P_max [mW] | 0.832 ± 0.025 | V_max [V] | 0.767 ± 0.011 |
| FF [%] | 72.8 ± 1.4 | Area [cm²] | 0.06730 ± 0.00050 |

| | |
|---|---|
| I_sc [A] | 0.001180 ± 0.000025 |
| I_max [A] | 0.001084 ± 0.000025 |
| M | 0.994 ± 0.015 |

**Methods:**
I-V: ASTM E948-16 *Standard Test Method for Electrical Performance of Photovoltaic Cells Using Reference Cells Under Simulated Sunlight*
QE: ASTM E1021-15 *Standard Test Method for Spectral Responsivity Measurements of Photovoltaic Devices*

**Standard Reporting Conditions:**
Spectrum: AM1.5-G (ASTM G173-03/IEC 60904-3 ed. 2)
1000.0 W/m² at 25.0°C

**Secondary Reference Cell:**
Device S/N: 10510-0054
Device Material: mono-Si
Window Material: fused silica
Certification: National Renewable Energy Laboratory
A2LA accreditation certificate # 2236.01
ISO Tracking #: 2008
Certified short circuit current ($I_{sc}$) under standard reporting conditions (SRC): 124.70 mA
Calibration due date: 26-Sep-21

**Solar Simulator:**
Spectrum: Newport Corporation filename *Sol3A_Spectroradiometer_Scan_0215.xls*
Total irradiance: 1000 W/m² based on $I_{sc}$ of the above Secondary Reference Cell

**Quantum Efficiency for DUT:**
Newport Corporation filename *QE 7226962, MM1, 0,11 mA WLB.log*
Spectral mismatch correction factor: M = 0.994 ± 0.015

**DUT Calibration Procedures:**
Newport Corporation document WI1 (EQE).docx
Newport Corporation document Area Measurement WI2 (Area).docx
Newport Corporation document WI3 (IV.Sweep).docx

| | | |
|---|---|---|
| Cal Cert V1.8 | Issue Date: May 15, 2020 | Page 2 of 2 |
| | Reviewed and Approved by: Geoffrey Wicks (Geoffrey.Wicks@mksinst.com) | |
| This certificate to be reproduced in part only with written permission from the Newport PV Laboratory | | |

Technology and Application Center
PV Lab
Calibration Number 2310

| | | |
|---|---|---|
| Cal Cert Data V1_2 | Issue Date: May 15, 2020 | Page 2 of 3 |
| | Reviewed and Approved by: Geoffrey Wicks<br>Geoffrey.Wicks@mksinst.com | |

Technology and Application Center
PV Lab
Calibration Number 2310

**Current-voltage parameters were measured under a 10-point IV sweep configuration wherein the bias voltage (current for Voc determination) is held constant until the measured current (voltage for Voc) is determined to be unchanging at the 0.07% level. This is intended to represent the quasi-steady-state performance of the device. Total IV measurement time under these conditions was approximately 11 minutes.**

| | | |
|---|---|---|
| Cal Cert Data V1_2 | Issue Date: May 15, 2020 | Page 1 of 3 |
| | Reviewed and Approved by: Geoffrey Wicks<br>Geoffrey.Wicks@mksinst.com | |

**Supplementary Fig. 25 | The photovoltaic performance certificate from Newport.** A beyond-Shockley-Queisser-limit $V_{OC}$ of 0.967 V has been recorded with a bandgap of 1.042 eV in a single-junction device. (**a**) The detailed report from Newport, where the Sn-based 2D perovskite (*n* = 5) serves as the absorber layer with an Au/PTAA/perovskite/ICBA/ITO structure. The certified $V_{OC}$ is 0.967 V under the quasi-steady-state condition. (**b**) The quantum efficiency plot of the certified device. The carrier collection cutoff (~1190 nm) in the plot indicates that the device bandgap is 1.042 eV. However, according to Shockley-Queisser-limit, the theoretical maximal $V_{OC}$ for such a photovoltaic is 0.802 V. (**c**) The I-V curve of the certified device under the quasi-steady-state, showing negligible hysteresis. This is because the high quality single crystal structure of the superlattice suppresses ion migration, reduce internal charge recombination, and eliminate accumulation of ions.

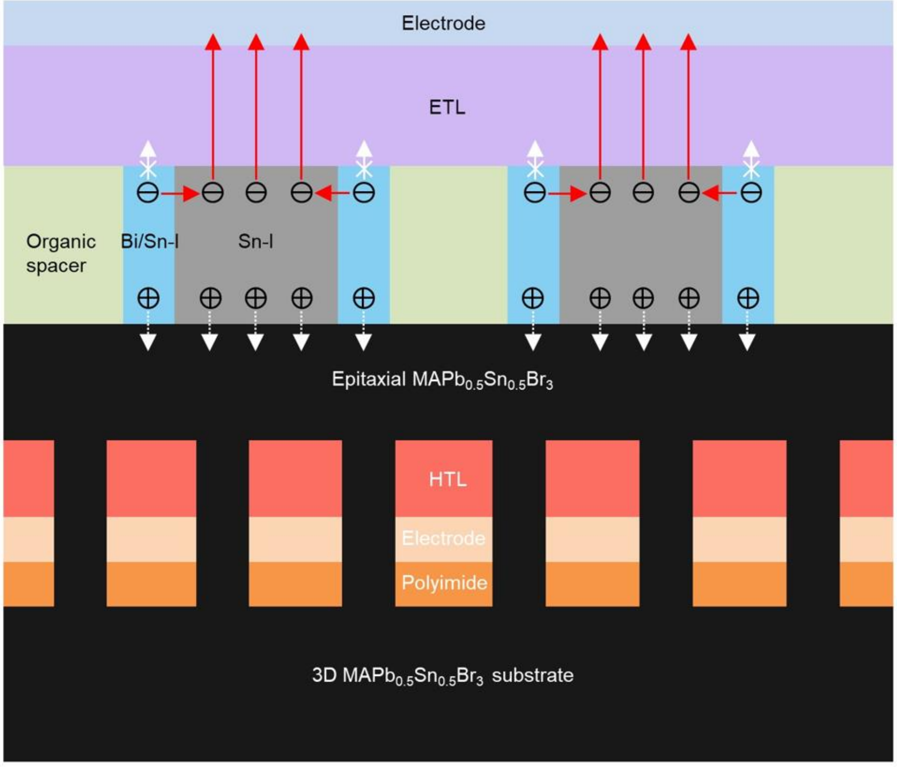

**Supplementary Fig. 26 | Schematics of the carrier transport in the superlattice photovoltaic device.** The patterned polyimide serves as the mask for epitaxial growth. A thin layer of $MAPb_{0.5}Sn_{0.5}Br_3$ (~200 nm) is first epitaxially grown on the $MAPb_{0.5}Sn_{0.5}Br_3$ substrate to provide uniform strain to the low-dimensional perovskites. The strained low-dimensional perovskite layer exhibits a vertical alignment to form a superlattice. In particular, the strain-induced $Bi^{3+}$ alloying creates two different band structures in the inorganic slabs (Bi/Sn-I and Sn-I), where the Bi/Sn-I shows a smaller bandgap with a lowered CBM. Due to the energy barrier between the Bi/Sn-I and the ETL layer, electrons are not likely to transport directly from the Bi/Sn-I to the ETL (white arrows). Instead, electrons are excited to high-energy states and diffuse to the Sn-I by intra-band relaxation and then transfer to the ETL (red arrows). Due to the energy barrier between the superlattice and the $MAPb_{0.5}Sn_{0.5}Br_3$ layer, holes are likely to accumulate/recombine at their interface to form band tail states. The holes could still be extracted by the hole transport layer to form a closed loop of charge flow.

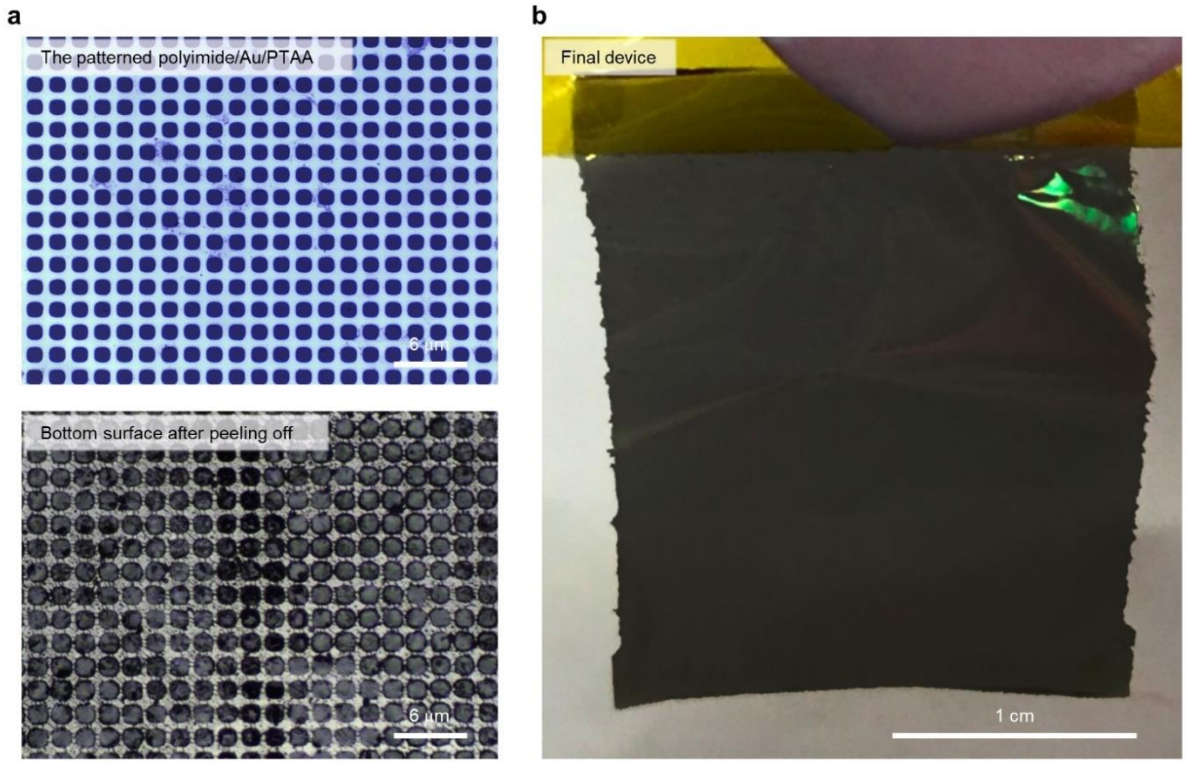

**Supplementary Fig. 27 | The *in-situ* fabricated flexible superlattice photovoltaics.** (**a**) Depositing Au and PTAA layers on the pre-patterned polyimide flexible mask to form a functionalized mask that can be directly used to fabricate devices without additional transfer of the perovskite layer. (**b**) The final device can be simply peeled off from the substrate without breaking the superlattice, suggesting the intrinsic flexibility of low-dimensional perovskites, where the soft organic spacers could serve as effective strain-releasing regions.

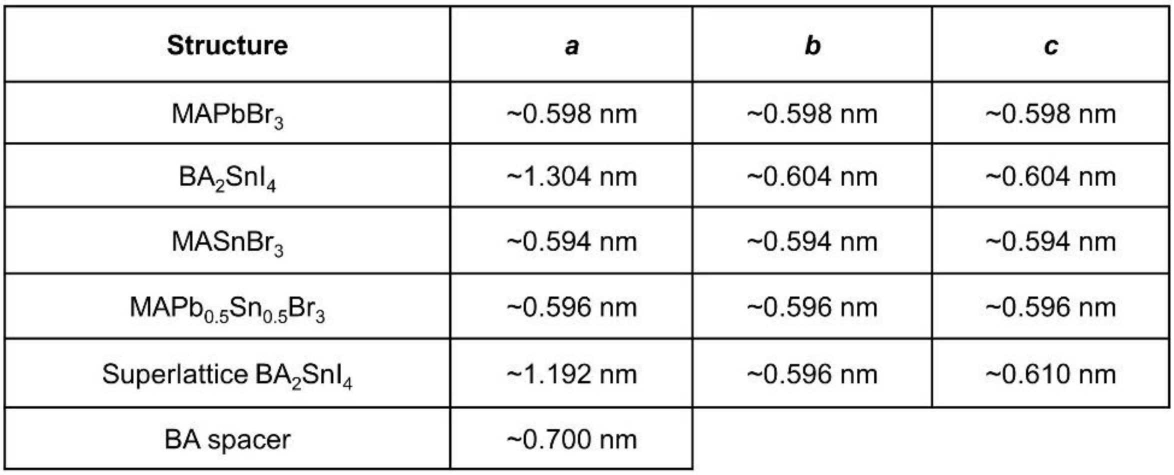

| Structure | *a* | *b* | *c* |
|---|---|---|---|
| $MAPbBr_3$ | ~0.598 nm | ~0.598 nm | ~0.598 nm |
| $BA_2SnI_4$ | ~1.304 nm | ~0.604 nm | ~0.604 nm |
| $MASnBr_3$ | ~0.594 nm | ~0.594 nm | ~0.594 nm |
| $MAPb_{0.5}Sn_{0.5}Br_3$ | ~0.596 nm | ~0.596 nm | ~0.596 nm |
| Superlattice $BA_2SnI_4$ | ~1.192 nm | ~0.596 nm | ~0.610 nm |
| BA spacer | ~0.700 nm | | |

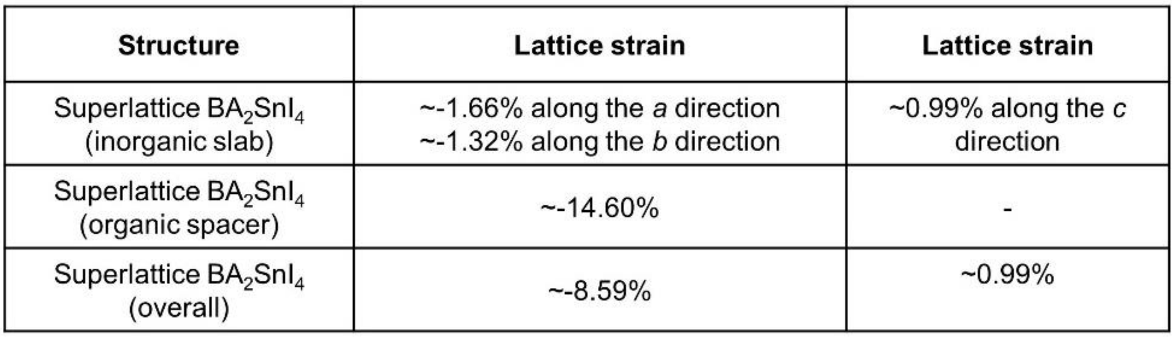

| Structure | Lattice strain | Lattice strain |
|---|---|---|
| Superlattice $BA_2SnI_4$ (inorganic slab) | ~-1.66% along the *a* direction<br>~-1.32% along the *b* direction | ~0.99% along the *c* direction |
| Superlattice $BA_2SnI_4$ (organic spacer) | ~-14.60% | - |
| Superlattice $BA_2SnI_4$ (overall) | ~-8.59% | ~0.99% |

**Supplementary Table 1. A summary of the lattice parameters and strains in the epitaxial growth process.** Those values are calculated from STEM and XRD results. Negative means compressive strain, and positive means tensile strain.

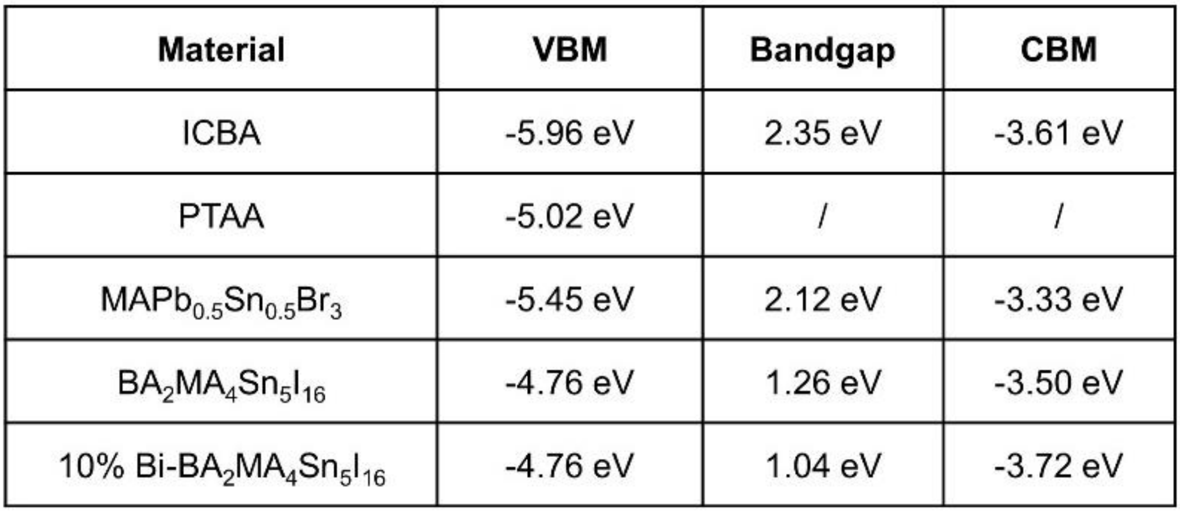

| Material | VBM | Bandgap | CBM |
|---|---|---|---|
| ICBA | -5.96 eV | 2.35 eV | -3.61 eV |
| PTAA | -5.02 eV | / | / |
| $MAPb_{0.5}Sn_{0.5}Br_3$ | -5.45 eV | 2.12 eV | -3.33 eV |
| $BA_2MA_4Sn_5I_{16}$ | -4.76 eV | 1.26 eV | -3.50 eV |
| 10% Bi-$BA_2MA_4Sn_5I_{16}$ | -4.76 eV | 1.04 eV | -3.72 eV |

**Supplementary Table 2. A summary of the band structure of the materials used in the certified photovoltaic device.** Those values are calculated from UV-Vis and UPS measurements.

# REFERENCES

1 Grancini, G. et al. Dimensional tailoring of hybrid perovskites for photovoltaics. *Nat. Rev. Mater.* **4**, 4-22 (2019).

2 Tsai, H. et al. High-efficiency two-dimensional Ruddlesden–Popper perovskite solar cells. *Nature* **536**, 312-316 (2016).

3 Stoumpos, C. C. et al. Ruddlesden–Popper hybrid lead iodide perovskite 2D homologous semiconductors. *Chem. Mater.* **28**, 2852-2867 (2016).

4 Wang, J. et al. Templated growth of oriented layered hybrid perovskites on 3D-like perovskites. *Nat. Commun.* **11**, 1-9 (2020).

5 Chen, A. Z. et al. Origin of vertical orientation in two-dimensional metal halide perovskites and its effect on photovoltaic performance. *Nat. Commun.* **9**, 1-7 (2018).

6 Zhang, X. et al. Vertically oriented 2D layered perovskite solar cells with enhanced efficiency and good stability. *Small* **13**, 1700611 (2017).

7 Yang, R. et al. Oriented quasi-2D perovskites for high performance optoelectronic devices. *Adv. Mater.* **30**, 1804771 (2018).

8 Zhang, X. et al. Orientation regulation of phenylethylammonium cation based 2D perovskite solar cell with efficiency higher than 11%. *Adv. Energy Mater.* **8**, 1702498 (2018).

9 Li, M. et al. Tin halide perovskite films made of highly oriented 2D crystals enable more efficient and stable lead-free perovskite solar cells. *ACS Energy Lett.* **5**, 1923-1929 (2020).

10 Liu, Y. et al. Surface-tension-controlled crystallization for high-quality 2D perovskite single crystals for ultrahigh photodetection. *Matter* **1**, 465-480 (2019).

11 Zheng, J.-Y. et al. Synthesis of centimeter-size free-standing perovskite nanosheets from single-crystal lead bromide for optoelectronic devices. *Sci. Rep.* **9**, 1-9 (2019).

12 Di, J. et al. Recent progress of two-dimensional lead halide perovskite single crystals: crystal growth, physical properties, and device applications. *EcoMat* **2**, e12036 (2020).

13 Chen, Y. et al. Strain engineering and epitaxial stabilization of halide perovskites. *Nature* **577**, 209-215 (2020).

14 Lei, Y. et al. Controlled Homoepitaxial Growth of Hybrid Perovskites. *Adv. Mater.* **30**, 1705992 (2018).

15 Lei, Y. et al. A fabrication process for flexible single-crystal perovskite devices. *Nature* **583**, 790-795 (2020).

16 Soe, C. M. M. et al. Structural and thermodynamic limits of layer thickness in 2D halide perovskites. *Proc. Natl. Acad. Sci.* **116**, 58-66 (2019).

17 Karmakar, A. et al. Cu (II)-doped Cs2SbAgCl6 double perovskite: A lead-free, low-bandgap material. *Chem. Mater.* **30**, 8280-8290 (2018).

18 Liu, S. et al. Manipulating efficient light emission in two-dimensional perovskite crystals by pressure-induced anisotropic deformation. *Sci. Adv.* **5**, eaav9445 (2019).

19 Blancon, J.-C. et al. Semiconductor physics of organic–inorganic 2D halide perovskites. *Nat. Nanotechnol.* **15**, 969-985 (2020).

20 Guo, S. et al. Pressure-Suppressed Carrier Trapping Leads to Enhanced Emission in Two-Dimensional Perovskite $(HA)_2(GA)Pb_2I_7$. *Angew. Chem.* **132**, 17686-17692 (2020).

21 Kong, L. et al. Highly tunable properties in pressure-treated two-dimensional Dion–Jacobson perovskites. *Proc. Natl. Acad. Sci.* **117**, 16121-16126 (2020).

22 Spanopoulos, I. et al. Uniaxial expansion of the 2D Ruddlesden–Popper perovskite family for improved environmental stability. *J. Am. Chem. Soc.* **141**, 5518-5534 (2019).

23 Ozaki, M. et al. Solvent-coordinated tin halide complexes as purified precursors for tin-based perovskites. *ACS Omega* **2**, 7016-7021 (2017).

24 Yao, Z. et al. Local temperature reduction induced crystallization of MASnI 3 and achieving a direct wafer production. *RSC Adv.* **7**, 38155-38159 (2017).

25 Cheng, B. et al. Extremely reduced dielectric confinement in two-dimensional hybrid perovskites with large polar organics. *Commun. Phys.* **1**, 1-8 (2018).

26 Wang, T. et al. Protecting hot carriers by tuning hybrid perovskite structures with alkali cations. *Sci. Adv.* **6**, eabb1336 (2020).

27 Fu, J. et al. Hot carrier cooling mechanisms in halide perovskites. *Nat. Commun.* **8**, 1-9 (2017).

28 Lei, Y. et al. Controlled Homoepitaxial Growth of Hybrid Perovskites. *Adv. Mater.* **30**, e1705992 (2018).